


TESS discovery of a super-Earth and two sub-Neptunes orbiting the bright, nearby, Sun-like star HD 22946

Luca Caciapuoti^{1,2} , Laura Inno^{3,4}, Giovanni Covone^{1,4,5}, Veselin B. Kostov⁶, Thomas Barclay^{6,42}, Elisa V. Quintana⁶, Knicole D. Colon⁶, Keivan G. Stassun^{7,8}, Benjamin Hord⁹, Steven Giacalone¹⁰, Stephen R. Kane¹¹, Kelsey Hoffman¹², Jason Rowe¹³, Gavin Wang¹⁴, Kevin I. Collins¹⁵, Karen A. Collins¹⁶, Thiam-Guan Tan^{17,39}, Francesco Gallo¹, Christian Magliano¹, Riccardo M. Ienco¹, Markus Rabus¹⁸, David R. Ciardi^{19,20}, Elise Furlan¹⁹, Steve B. Howell²¹, Crystal L. Gnilka²¹, Nicholas J. Scott²¹, Kathryn V. Lester²¹, Carl Ziegler²², César Briceño²³, Nicholas Law²⁴, Andrew W. Mann²⁴, Christopher J. Burke²⁵, Samuel N. Quinn²⁶, Angelo Ciaramella³, Pasquale De Luca³, Stefano Fiscale³, Alessandra Rotundi³, Livia Marcellino³, Ardelio Galletti³, Ida Bifulco³, Fabrizio Oliva²⁷, Alton Spencer²⁸, Lisa Kaltenegger²⁹, Scott McDermott³⁰, Zahra Essack^{31,32}, Jon M. Jenkins²¹, Bill Wohler^{12,33}, Joshua N. Winn³⁴, S. Seager^{25,35,36}, Roland Vanderspek²⁵, George Zhou³⁷, Avi Shporer³⁸, Diana Dragomir⁴⁰, and William Fong⁴¹

(Affiliations can be found after the references)

Received 16 March 2022 / Accepted 14 September 2022

ABSTRACT

We report the Transiting Exoplanet Survey Satellite (TESS) discovery of a three-planet system around the bright Sun-like star HD 22946 ($V \approx 8.3$ mag), also known as TIC 100990000, located 63 pc from Earth. The system was observed by TESS in Sectors 3, 4, 30, and 31 and two planet candidates, labeled TESS Objects of Interest (TOIs) 411.01 (planet *c*) and 411.02 (planet *b*), were identified on orbits of 9.57 and 4.04 days, respectively. In this work, we validate the two planets and recover an additional single transit-like signal in the light curve, which suggests the presence of a third transiting planet with a longer period of about 46 days. We assess the veracity of the TESS transit signals and use follow-up imaging and time-series photometry to rule out false-positive scenarios, including unresolved binary systems, nearby eclipsing binaries, and contamination of the light curves by background or foreground stars. Parallax measurements from *Gaia* Early Data Release 3 together with broad-band photometry and spectroscopic follow-up by the TESS FollowUp Observing Program (TFOP) allowed us to constrain the stellar parameters of TOI-411, including its radius of $1.157 \pm 0.025 R_{\odot}$. Adopting this value, we determined the radii for the three exoplanet candidates and found that planet *b* is a super-Earth with a radius of $1.48 \pm 0.06 R_{\oplus}$, while planets *c* and *d* are sub-Neptunian planets with radii of $2.35 \pm 0.08 R_{\oplus}$ and $2.78 \pm 0.13 R_{\oplus}$ respectively. Using dynamical simulations, we assessed the stability of the system and evaluated the possibility of the presence of other undetected, non-transiting planets by investigating its dynamical packing. We find that the system is dynamically stable and potentially unpacked, with enough space to host at least one more planet between *c* and *d*. Finally, given that the star is bright and nearby, we discuss possibilities for detailed mass characterisation of its surrounding worlds and opportunities for the detection of their atmospheres with the *James Webb* Space Telescope.

Key words. planets and satellites: fundamental parameters – planets and satellites: general – planets and satellites: detection

1. Introduction

Multi-planetary systems are crucial cosmic environments with which to probe our theories of planet formation and evolution. Exoplanet surveys have revealed an unexpected diversity of such systems, including exoplanets for which no analog is present in the Solar System and planetary systems whose orbital architecture is very different from that of our own (see e.g., Gillon et al. 2017; Naef et al. 2001; Winn et al. 2011; Miret-Roig et al. 2022). Transiting planetary systems around nearby, bright stars offer the opportunity for in-depth observational studies to characterize different planets formed in a common environment. The Transiting Exoplanet Survey Satellite (TESS; Ricker et al. 2015) is a space-borne NASA mission launched in 2018 to survey the sky for transiting exoplanets around these stars. To date, it has contributed to the discovery of more than 200 exoplanets in the Galaxy, with more than 5700 candidates on hold

for confirmation¹. These discoveries include planets of different sizes, ranging from Mars-like bodies (e.g., L98-59 *b*, Kostov et al. 2019) to gas giants larger than Jupiter (e.g., TOI-640 *b*, Rodriguez et al. 2021), with the majority of them being super-Earths ($1.25 < R_{\oplus} < 1.75$) and sub-Neptunes ($1.75 < R_{\oplus} < 3.5$), according to the classification criteria defined by Fulton et al. (2017).

Exoplanets discovered around bright stars are ideal targets for detailed characterization, including the measurements of their mass via Doppler spectroscopy and the determination of their atmospheric properties through transmission or emission spectroscopy. Furthermore, multiplanetary systems offer the additional opportunity to perform comparative exoplanetology studies, as we can constrain the formation and evolution of a

¹ See the NASA Exoplanet Archive at <https://exoplanetarchive.ipac.caltech.edu/>

group of planets that share a common origin given the fixed properties of the host star. For these systems, we can gather enough information to constrain the orbits and dynamics of the system, and hence to infer the underlying formation and evolution scenarios; see for example Ragozzine & Holman (2010); Lissauer et al. (2011); Fabrycky et al. (2014).

In this work, we report the TESS discovery of a multi-planetary system consisting of a super-Earth and two sub-Neptune-sized planets orbiting the bright ($V \approx 8.3$ mag), nearby (63 pc), Sun-like star HD 22946, indicated in the TESS Input Catalog (Stassun & Torres 2018) as TIC 100990000 and as TOI-411 in the TESS Objects of Interest (TOI) list on ExoFOP-TESS².

Sub-Neptunes and super-Earths are of particular interest for planetology studies because, while they represent the highest fraction of planets detected in the Galaxy, they are not observed in the Solar System. The detection and in-depth characterization of such planets orbiting Sun-like stars can help us constrain the formation and evolution pathways along which they form and gain a better understanding of different planetary systems (Bitsch 2019). For example, a depression in the distribution of exoplanet radii between 1.5 and $2R_{\oplus}$ (Fulton et al. 2017; Owen & Wu 2017) seems to indicate that these exoplanets accreted an atmosphere at the time of formation that progressively thinned out due to heat-driven processes, such as stellar radiation photo-evaporation (Fulton & Petigura 2018) or core-powered mass loss (Ginzburg et al. 2018). Moreover, Loyd et al. (2020) found that doubling the known sample of exoplanets with radii $R < 4R_{\oplus}$ is required to confirm or exclude the role of photo-evaporation in the supposed atmospheric loss of these worlds. Therefore, by studying planets in this range, we can shed light on the physical processes that can lead to the loss of a primary atmosphere and the possible accretion of a heavier secondary one.

The paper is organized as follows. In Sect. 2, we characterize the host star, in Sect. 3 we present the detection of the three transiting candidates from TESS observations and their characterization. In Sect. 4, we analyze the follow-up data to validate their planetary nature. In Sect. 5, we explore the dynamics of the system and the potential for atmospheric characterization of its planets. Finally, in Sect. 6, we summarize our findings.

2. Characterization of the host star

Characterizing the physical properties of the host star, such as its mass, M_{\star} , radius, R_{\star} , and effective temperature, T_{eff} , is propaedeutic to constraining the corresponding properties of its planetary system. Therefore, we first focus on determining these quantities for HD 22946, together with its spectral class, surface gravity, $\log g$, metallicity, $[\text{Fe}/\text{H}]$, and sky-projected rotational velocity, $v \sin i$.

HD 22946 is a bright ($V \approx 8.3$ mag) main sequence star located in the Southern Hemisphere, characterized by a high proper motion and some photometric variability. Basic stellar information is given in Table 1.

2.1. Stellar variability

In order to better understand the photometric variability of the star, we searched for publicly available light curves of HD 22946; we only found multi-epoch photometry from the HIPPARCOS Epoch Photometry catalog (Hip 1997), which

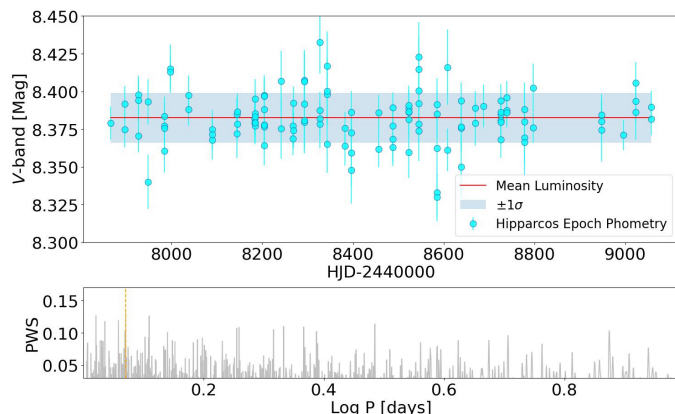


Fig. 1. Light curve of HD 22946 from the HIPPARCOS Epoch Photometry data (V -band, *top panel*), and the corresponding power spectrum (*bottom panel*). In the *top panel*, the mean luminosity and standard deviation are also shown: the scatter in the photometric data is compatible with a low-amplitude variability. The peak of the power spectrum, indicated by the orange vertical line, is found at ≈ 0.073 days, and it is likely due to instrumental aliasing.

includes 100 measurements over about 3 yr, with 3–10 measurements per night each month³.

The light curve from the HIPPARCOS data shows a small-amplitude variation, with a maximum–minimum difference of about ≈ 0.1 mag, or six times the standard deviation σ of the measurements, as can be seen in Fig. 1; we also show the computed Lomb–Scargle (Lomb 1976; Scargle 1982) periodogram using a Nyquist factor of 10 following a recommendation from Richards et al. (2012) and VanderPlas (2018). The peak of the power spectrum is found at around 0.073 days, close to the 0.076 days data gaps of HIPPARCOS observations (Percy et al. 2002), and therefore it is likely due to aliasing. Indeed, the star is classified as static (class “C”) in the HIPPARCOS catalog. The TESS light curve of HD 22946 also shows mild signs of variability, especially in sectors 30 and 31, which are described in more detail in the following section.

2.2. Stellar parameters

Light curves from photometric transits only allow the measurement of the planet-to-star radius ratio, and therefore we need to accurately determine the stellar radius in order to infer the radii of the transiting planets. In the literature, there are several estimates for the mass and radius of HD 22946: (i) the values from *Gaia* DR2 (Gaia Collaboration 2018), and (ii) the values obtained by Kervella et al. (2019, hereinafter K19) using the $V, V-K$ surface brightness relations for the radius (Kervella et al. 2004) and the isochrone fitting method for the mass (Girardi et al. 2000). Both these approaches depend on the measured parallax. In addition to these estimates, we can use two different and independent methods to infer the radius of the star and the other stellar parameters. The first method relies on the analysis of the spectra collected through the TESS Followup Observing Program (TFOP⁴, Collins 2019): high-resolution, high

² <https://exofop.ipac.caltech.edu/tess/>

³ Light curves for this star are available in the ASAS-SN Sky Patrol database (Shappee et al. 2014; Jayasinghe et al. 2021, and references therein) and in ASAS (Pojmanski 1997), but the stellar magnitude is close to the surveys’ saturation limit, and so we discarded this data. Epoch photometry from *Gaia* DR3 is not available for this star.

⁴ <https://tess.mit.edu/followup/>

Table 1. Summary of stellar data used in this work.

Parameters	Value	Source
Name	TOI-411	Guerrero & TESS Science Office (2021)
TIC ID	100990000	TICv8.1
Alt. name	HD 22946	
Astrometric properties		
α RA (hh:mm:ss)	03:39:16.761	<i>Gaia</i> EDR3
δ Dec (dd:mm:ss)	−42:45:45.185	<i>Gaia</i> EDR3
μ_α (mas yr ^{−1})	−51.618 ± 0.015	<i>Gaia</i> EDR3
μ_δ (mas yr ^{−1})	−110.546 ± 0.021	<i>Gaia</i> EDR3
Barycentric V_{rad} (km s ^{−1})	16.91 ± 0.15	<i>Gaia</i> DR2
Distance (pc)	62.87 ± 0.05	<i>Gaia</i> EDR3
Photometric data		
TESS (mag)	7.757 ± 0.006	TIC v8.1
FUV (mag)	19.45 ± 0.16	GALEX GR6
NUV (mag)	13.014 ± 0.005	GALEX GR6
B_T (mag)	8.903 ± 0.017	<i>Tycho-2</i>
V_T (mag)	8.318 ± 0.012	<i>Tycho-2</i>
G -band (mag)	8.1281 ± 0.0003	<i>Gaia</i> DR2
G_{BP} -band (mag)	8.4206 ± 0.0003	<i>Gaia</i> DR2
G_{RP} -band (mag)	7.7173 ± 0.0003	<i>Gaia</i> DR2
B (mag)	8.79 ± 0.03	TIC v8.1
V (mag)	8.27 ± 0.03	TIC v8.1
J (mag)	7.25 ± 0.04	2MASS
H (mag)	7.04 ± 0.04	2MASS
K_s (mag)	6.98 ± 0.03	2MASS
w_1 (mag)	6.91 ± 0.04	WISE
w_2 (mag)	6.93 ± 0.02	WISE
w_3 (mag)	6.95 ± 0.02	WISE
w_4 (mag)	6.86 ± 0.05	WISE
Spectroscopic data in TFOP		
UT 2019-02-09	$S/N = 34$	NRES at LCO
UT 2019-02-19	$S/N = 40$	NRES at LCO
UT 2019-02-23	$S/N = 40$	NRES at LCO
UT 2019-02-27	$S/N = 41$	NRES at LCO
UT 2019-02-23	$S/N = 86$	CHIRON at SMARTS
UT 2019-08-09	$S/N = 70$	CHIRON at SMARTS
UT 2021-01-10	$S/N = 63$	CHIRON at SMARTS
UT 2021-08-28	$S/N = 50$	CHIRON at SMARTS

signal-to-noise-ratio (S/N) optical spectra of HD 22946 were taken at four different epochs with both the Network of Robotic Echelle Spectrographs of the Las Cumbres Observatory (NRES and LCO; Siverd et al. 2018, 2016; Brown et al. 2013) and the CHIRON spectrograph (Tokovinin 2018) on the 1.5 m Small and Moderate Aperture Research Telescope System (SMARTS) at the Cerro Tololo Inter-American Observatory (CTIO).

The observations are detailed in Table 1. NRES data cover a 380–860 nm spectral band with a resolution of 53 000 and were processed by the dedicated data-reduction pipeline (McCully et al. 2018), and then analyzed using SpecMatch (Petigura et al. 2017). CHIRON spectra cover the 450–890 nm range with a resolution of 80 000. The spectra were collected by the instrument team and reduced following the optimal extraction method described in Paredes et al. (2021). We derived radial velocities by fitting the line profiles of the spectra, which were extracted via least squares deconvolution (LSD) of the observed spectrum

against synthetic templates (Donati et al. 1997), and we estimated the spectroscopic stellar parameters using the gradient-boosting regressor implemented in the scikit-learn Python module, previously trained on spectra classified by SPC (Buchhave et al. 2012). Our analysis of the line profiles reveals negligible rotational broadening and no evidence of double lines, suggesting that the star is inactive and not a host to unresolved, close-in stellar companions.

Table 2 lists the radial velocity V_{rad} measured at each epoch, and the weighted average with associated uncertainties for all the stellar parameters obtained by the spectral analysis with the prior of the *Gaia* parallax. We note that the V_{rad} measured at the different epochs from the same spectrograph are all consistent with each other. A zero-point discrepancy among the measurements obtained from the two instruments is expected. NRES observations do not show significant variation at the level of 600 m s^{−1} over 18 days while CHIRON spectra do not show significant variation at the level of 100 m s^{−1} over 2.5 yr^{−1}. Moreover, the

Table 2. Stellar data.

Parameter	Value	Source
	Literature Data	
T_{eff} (K)	6115 ± 324	<i>Gaia</i> DR2
A_G (mag)	0.05 ± 0.5	<i>Gaia</i> DR2
V_{rad} (km s ⁻¹)	16.91 ± 0.15	<i>Gaia</i> DR2
R_{\star} (R_{\odot})	1.14 ± 0.11	<i>Gaia</i> DR2
M_{\star} (M_{\odot})	1.158 ± 0.058	K19
R_{\star} (R_{\odot})	1.115 ± 0.056	K19
V_{rad} (km s ⁻¹)	16.15 ± 0.04	Pribulla et al. (2014)
$v \sin i$ (km s ⁻¹)	7.05 ± 0.2	Pribulla et al. (2014)
Spectral type	F7/F8V	Pribulla et al. (2014)
	High-resolution spectroscopy	
V_{rad} (km s ⁻¹)	16.6 ± 0.3	NRES at LCO
V_{rad} (km s ⁻¹)	16.2 ± 0.3	NRES at LCO
V_{rad} (km s ⁻¹)	16.5 ± 0.8	NRES at LCO
V_{rad} (km s ⁻¹)	16.8 ± 0.4	NRES at LCO
V_{rad} (km s ⁻¹)	17.589 ± 0.033	CHIRON at SMARTS
V_{rad} (km s ⁻¹)	17.624 ± 0.022	CHIRON at SMARTS
V_{rad} (km s ⁻¹)	17.685 ± 0.038	CHIRON at SMARTS
V_{rad} (km s ⁻¹)	17.620 ± 0.037	CHIRON at SMARTS
T_{eff} (K)	$6210 \pm^{173}_{158}$	This work, NRES
$\log g$	4.4 ± 0.2	This work, NRES
[Fe/H]	$-0.05 \pm^{0.08}_{-0.05}$	This work, NRES
$v \sin i$ (km s ⁻¹)	3.4 ± 0.9	This work, NRES
M_{\star}	1.104 ± 0.012	This work, NRES
R_{\star}	1.157 ± 0.025	This work, NRES
T_{eff} (K)	6026 ± 50	This work, CHIRON
$\log g$	4.22 ± 0.10	This work, CHIRON
[Fe/H]	-0.22 ± 0.08	This work, CHIRON
$v \sin i$ (km s ⁻¹)	3.2 ± 0.5	This work, CHIRON
	SED fitting from broad-band photometry	
A_V	0.02 ± -0.01	This work
F_{bol} (erg s ⁻¹ cm ⁻²)	1.289 ± 0.030	This work
R_{\star} (R_{\odot})	1.139 ± 0.035	This work
M_{\star} (M_{\odot})	1.12 ± 0.06	from $\log g$ and R_{\star}
M_{\star} (M_{\odot})	1.13 ± 0.12	from Torres et al. (2010)'s empirical relations
Age (Gyr)	5 ± 1	This work
	Best values adopted throughout this work	
T_{eff} (K)	6040 ± 48	This work
$\log g$	4.26 ± 0.15	This work
[Fe/H]	-0.14 ± 0.07	This work
R_{\star} (R_{\odot})	1.157 ± 0.025	This work
M_{\star} (M_{\odot})	1.104 ± 0.012	This work

V_{rad} from *Gaia* DR2 also shows a small uncertainty, that is, a small rms from the different epoch observations, and is consistent with the value measured from the NRES spectra. All the above evidence further confirms that the star does not have a bound companion.

The second method used to obtain stellar parameters is based on the fitting of the spectral energy distribution (SED), that is, the flux emitted by the star across a broad wavelength range, which yields a semi-empirical determination of the stellar radius, mass, and age. We used the photometric data listed in Table 1, following the method described in

Stassun & Torres (2016, 2018). We retrieved public photometric data in different passbands as follows:

(i) Far- and near-ultraviolet (FUV and NUV) magnitudes from the GALEX catalog; (ii) BV magnitudes from the catalog of Mermilliod (2006); (iii) $B_T V_T$ magnitudes from the *Tycho-2* catalog; (iv) $GG_{\text{BP}}GR_{\text{P}}$ magnitudes from *Gaia* EDR3; (v) JHK_S magnitudes from the 2MASS catalog (Skrutskie et al. 2006; Cutri et al. 2003); and (vi) magnitudes in the mid-infrared (MIR) bands at 3.4, 4.6, 12, and 22 μm from the WISE catalog (Wright et al. 2010). The full wavelength range covered by the data goes from 0.15 to 22 μm , as shown in Fig. 2.

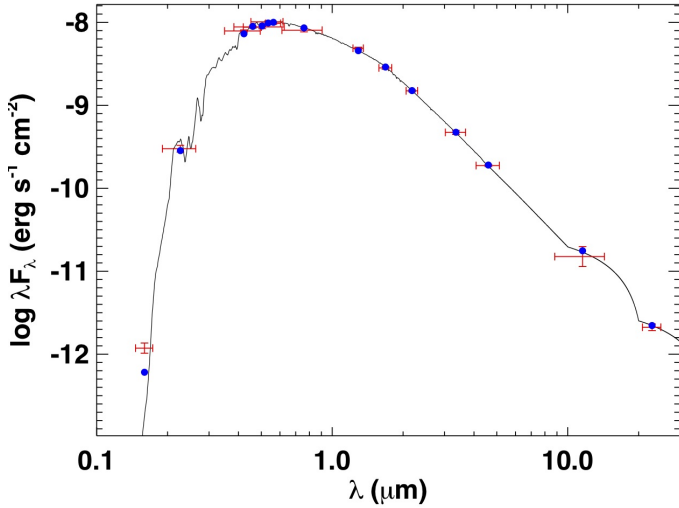


Fig. 2. Spectral energy distribution of HD 22946. The blue symbols and their vertical error bars represent the photometric measurements available for this source and listed in Table 1. The horizontal bars indicate instead the width of the passband for each data point. The overplotted black line is the best-fit model, which allows us to derive the stellar parameters.

We performed a fit using the Kurucz stellar atmosphere models, adopting the spectroscopically determined T_{eff} , $\log g$, and $[\text{Fe}/\text{H}]$, as well as the $v \sin i$ from Pribulla et al. (2014). The remaining free parameter is the interstellar extinction, A_V , which we limited to the maximum line-of-sight value from the dust maps of Schlegel et al. (1998). The fit is reasonably good, with a reduced χ^2 of 1.9 and best fit $A_V = 0.02 \pm 0.01$. Integrating the (unreddened) SED gives $F_{\text{bol}} = 1.289 \pm 0.030 \times 10^{-8} \text{ erg s}^{-1} \text{ cm}^{-2}$, which, combined with the *Gaia* EDR3 parallax (with no offset applied; see, e.g., Stassun & Torres 2021), gives $R_{\star} = 1.139 \pm 0.035 R_{\odot}$. With the spectroscopic $\log g$, we then calculate a value of $M_{\star} = 1.13 \pm 0.12 M_{\odot}$, which is consistent with that determined by adopting the Torres et al. (2010) empirical relations, namely $M_{\star} = 1.12 \pm 0.06 M_{\odot}$. Finally, we can estimate the stellar rotation period via the observed R'_{HK} activity index (Murgas et al. 2013) and the empirical rotation–activity relations of Mamajek & Hillenbrand (2008), which yields $P_{\text{rot}} = 10.6 \pm 0.9$ days. Using these rotation and activity measurements together with the activity–age relations of Mamajek & Hillenbrand (2008) gives an estimated stellar age of $\tau_{\star} = 5 \pm 1$ Gyr.

The derived stellar parameters from both methods are consistent with each other and listed in Table 2, together with the best values adopted through the next steps of the analysis, which were obtained by performing the error-weighted average of all the available parameters. In summary, we find that HD 22946 is a late-type F main sequence star, with $T_{\text{eff}} = 6040 \pm 48$ K, $\log g = 4.26 \pm 0.15$ dex, $[\text{Fe}/\text{H}] = -0.14 \pm 0.07$ dex, $M_{\star} = 1.104 \pm 0.012 M_{\odot}$, and $R_{\star} = 1.157 \pm 0.025 R_{\odot}$.

3. Discovery and characterization of HD 22946 planets

In this section, we present the TESS observations of HD 22946 and the analysis performed to detect and characterize the transit signals in its light curve.

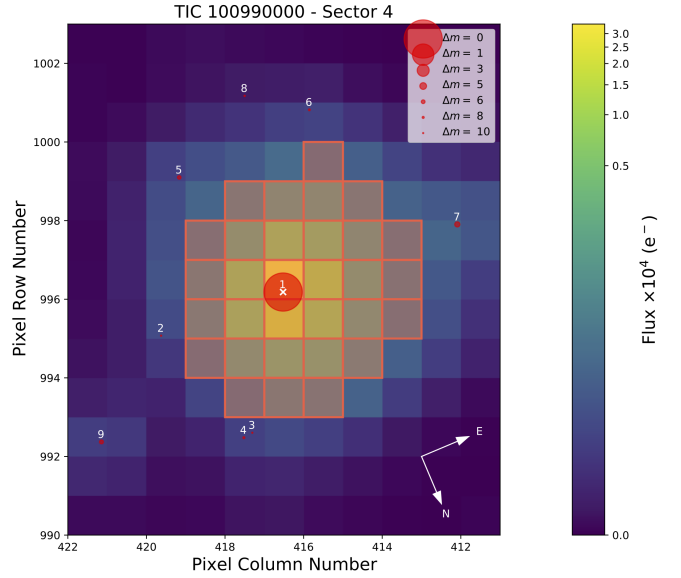


Fig. 3. TESS image of HD 22946 taken during Sector 4 observations. The target is in the center, labeled with a “1” an white cross. Nearby sources down to +10 mag are shown as smaller red dots and labeled in order of distance from the target. The SPOC-based optimal aperture for the specific sector is overplotted in red. The color scheme represents the flux scale on the pixels. This image has been created using the *tpfplotter* Python package (Aller et al. 2020).

3.1. TESS observations

TESS observed HD 22946 with Camera 3 in sectors 3 and 4 (2018 September 20 to 2018 October 18 and 2018 October 18 to 2018 November 15) during its primary mission and sectors 30 and 31 (2020 September 22 to 2020 October 21 and 2020 October 21 to 2020 November 19) during the extended mission. Figure 3 displays a single TESS frame of HD 22946 taken during Sector 4 observations. The first planet search was carried out with the Science Processing Operation Center (SPOC) pipeline (Jenkins et al. 2016), which is designed to identify potential exoplanet transits using a wavelet-based, adaptive noise-compensating matched filter. Subsequently, it fits a transit model to the detected signals (Li et al. 2019) and automatically performs a suite of tests to vet their planetary nature (Twicken et al. 2018). These are then collected in a data validation report (DVR), which is made available on both the ExoFOP-TESS and MAST⁵ archives. At this point, the pipeline masks the detected signals and runs from the top to identify new signatures. It stops after eight tries or in cases where the latest found signal is below a certain S/N threshold. Finally, the pipeline generates two different light curves for the detected TOIs: the first one is extracted through simple-aperture photometry (SAP-FLUX; Twicken et al. 2010; Morris et al. 2020), whilst the second has an additional pre-search data conditioning procedure (PDCSAP-FLUX; Stumpe et al. 2014). This final step removes long-term trends and contamination due to nearby stars. Two planet candidates were discovered during this preliminary analysis and added as TESS TOI-411.01 and 411.02 to ExoFOP-TESS. These candidates have periods of 9.57 days and 4.04 days, with transit epochs at 1385.72367 and 1386.189174 Barycentric TESS Julian Date (BTJD⁶), respectively. The full TESS light curve is shown in Fig. 4. The transits of the candidates are highlighted.

⁵ <https://mast.stsci.edu/>

⁶ BTJD = BJD-2457000.0

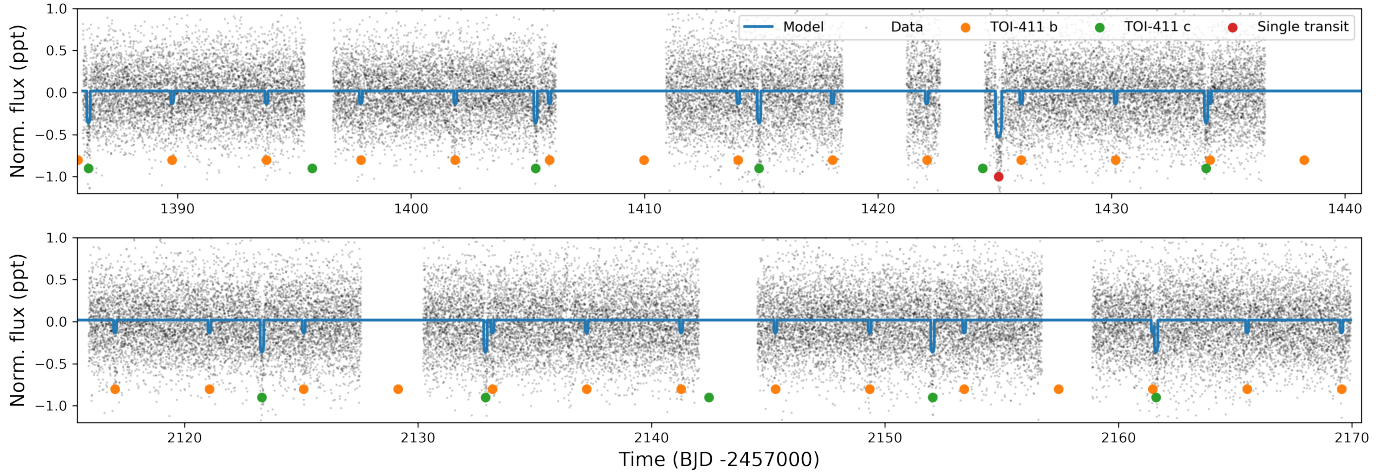


Fig. 4. Full light curve of TESS sectors 3, 4 (*top panel*), 30, and 31 (*bottom panel*). The blue line is the best-fit model. The transits of planets *b* and *c* are highlighted with orange and green dots, respectively. The single transit event is highlighted with a red dot.

3.2. Light-curve analysis

We downloaded and worked on the PDCSAP light curve for TOI-411 using the `lightkurve` package (Lightkurve Collaboration 2018). This code makes use of an automatically generated optimal aperture but we checked that different tentative choices of aperture around this target do not affect the depth of the transit signals. Starting with this time series, we first recover the candidate events and subsequently fit them to retrieve physical and orbital parameters.

3.3. Candidate detection

We used the Transit Least Squares (TLS) package (Hippke & Heller 2019) to recover the candidate signals. This code allows searches for periodic, transit-like signals in a light curve by brute-force fitting templates of transits built over a grid of parameters. We decided to adopt this code with respect to the more commonly used Box Least Squares (BLS, Kovács et al. 2002) algorithm, because it also accounts for the effect of stellar limb darkening on the shape of transits, and, according to the authors, this improvement yields a $\sim 10\%$ higher detection efficiency (and 10% lower false-alarm rates) compared to BLS, which is especially relevant for low-S/N signals. The brute-force fitting consists of the phase-folding of the light curve over a grid of trial periods, transit epochs, and duration, and computing the χ^2 at each solution. The solution is then found by minimizing the χ^2 . The period grid is a uniformly spaced set of N possible values within a given range. The upper limit of the range is set by the minimum number of transits we want to find over the entire observation window, which we set to two. The lower limit is such that the candidate orbits just wide of the Roche limit of its star (in the assumption of a planet density of $\rho_p = 1 \text{ g cm}^{-3}$). In the case of HD 22946, this limit corresponds to 0.6 days. We performed the first TLS run independently on the couples of sectors [3,4] and [30,31] to ease the computational burden of the search. The first run on sectors 3 and 4 yields a periodic event with a period of ~ 9.57 days, which is consistent with the ExoFOP TESS listed period for TOI-411.01. Masking this signal and running a second search, we recover the events associated with TOI-411.02 on a ~ 4.04 -day period. A third TLS run does not return consistent periodic events. The same results are found for sectors 30 and 31. In addition, by visually inspecting the available sectors, we notice two additional events: a transit-like feature in sector 4

at BTJD ~ 1425 and another dip in sector 30 at BTJD ~ 2136.5 . However, the latter event presents an asymmetric shape and it overlaps the momentum dump reported in TESS Data Release Notes no.45 (DRN45, and Figs. 4 and 7 therein) on MAST⁷ at the same epoch. The former event, instead, does not correspond to any reported spacecraft maneuver epoch. Hence, we only consider the sector 4 transit-like signal hereafter. This newly found signal is then a single event candidate exoplanet whose period is yet to be defined (see Fig. 4 of this work). This single event candidate was also recently reported independently on ExoFOP-TESS (as TIC 100990000.03) by A.S., a member of the Planet Hunters TESS citizen science project (Eisner et al. 2021). We note that TESS is not scheduled to observe this target again during its upcoming extended mission and therefore follow-up observations with other facilities will be needed to confirm this newly found candidate exoplanet.

3.4. Transit modeling

We used `exoplanet`, a code for probabilistic modeling of exoplanet transits (Foreman-Mackey et al. 2021), to measure the properties of the transiting planets. The model we set up consists of four elements: three planet transit components with Keplerian orbits and limb-darkened transits, and a Gaussian Process (GP) component that models residual stellar variability. We combined the data from all the sectors into one time series with the same median normalized brightness. The planet models were computed with `exoplanet` using STARRY (Luger et al. 2019), while the GP was computed using `celerite` (Foreman-Mackey et al. 2017; Foreman-Mackey 2018). The GP component is described as a stochastically driven, damped harmonic oscillator with parameters of $\log(S_0)$ and $\log(\omega_0)$, where the power spectrum of the GP is

$$S(\omega) = \sqrt{\frac{2}{\pi}} \frac{S_0 \omega_0^4}{(\omega^2 - \omega_0^2)^2 + \omega^2 \omega_0^2 / Q^2}, \quad (1)$$

and a white noise term, with a model parameter of the log variance. We fixed Q to one-third and put wide Gaussian priors on $\log(S_0)$ and $\log(\omega_0)$ with means of the log variance, and one log of one-tenth of a cycle, respectively, and a standard deviation on the priors of 10. This form of GP was chosen because it

⁷ https://archive.stsci.edu/tess/tess_drn.html

enables us to model a wide range of low-frequency astrophysical and instrumental signals without requiring a physical model for the observed variability. The white noise term carried the same prior as $\log(S_0)$. The planet model was parameterized in terms of limb darkening, log stellar density, and stellar radius for the three planets. Each individual planet was parameterized in terms of log orbital period, time of transit, planet-to-star radius ratio, impact parameter, orbital eccentricity, and periastron angle at the time of transit. The time of transit was set to a transit near the center of the time series to minimize correlations between transit epoch and orbital period. The stellar radius had a Gaussian prior of $1.157 \pm 0.025 R_\odot$. The log mean stellar density, in cgs units, had a Gaussian prior with a mean of $\log 1.1$ and standard deviation of 0.18 dex. The limb darkening followed the [Kipping \(2013\)](#) parameterization. The log orbital periods, time of transit, and log planet-to-star radius ratio of the three candidates had Gaussian priors with means at the values listed on ExoFOP-TESS (aside from the single transiting planet where we fixed the orbital period). The impact parameter had a uniform prior of between zero and one plus the planet-to-star radius ratio. Eccentricity had a beta prior with $\alpha = 0.867$ and $\beta = 3.03$ (as suggested by [Kipping 2013](#)), and was bounded between zero and one. The periastron angle at transit was sampled in vector space to avoid the sampler seeing a discontinuity at values of π . We sampled the posterior distribution of the model parameters using the No U-turn Sampler (NUTS, [Hoffman & Gelman 2014](#)) which is a form of Hamiltonian Monte Carlo, as implemented in PyMC3 ([Salvatier et al. 2016](#)). We ran four simultaneous chains, with 3000 tuning steps, and 2000 draws in the final sample. The phase-folded transits of the three candidates, along with best-fitting transit models, are shown in Fig. 5, and the model parameters are provided in Table 4. We note that, by using the transit duration and depth along with stellar mass and radius, we can estimate the period through Kepler’s third law in the assumption of planar and circular orbit, as shown in Sect. 6.5 of [Seager & Mallén-Ornelas \(2003\)](#). This yields a period of approximately 46 ± 4 days. A period of between 43 and 46 days would also be consistent with the possible overlap of a secondary transit corresponding to momentum dump in sector 30, with a missing signal that would fall in the downlink gap of sector 31 and just short of the beginning of observations for sector 3. Moreover, if we assume that the signal at BJD 2136.5 is a secondary transit happening at the same time as the reported momentum dump in sector 30, we find a period of 44.47 days, which is also consistent with our rough estimate. On the basis of TESS data only, we are not able to establish whether the signal that we observed in sector 30 at BJD 2136.5 is only due to an instrumental artifact or also includes the transit of planet *d*.

3.5. Additional radial-velocity data

By searching the ESO archive, we found that TOI-411 was observed by the Echelle SPectrograph for Rocky Exoplanets and Stable Spectroscopic Observations (ESPRESSO; [Pepe et al. 2014](#)) between 2019 February 20 and 2019 March 17 (program ID: 0102.C-0456; PI: Van Eylen). ESPRESSO is a high-resolution ($R \sim 140\,000$) spectrograph operating at the VLT at ESO’s Paranal Observatory, and is capable of measuring radial velocities of bright stars ($V < 8$ mag) with a precision of 10 cm s^{-1} in the 377–790 nm range. TOI-411 was observed 14 times in roughly one month, with typical exposure of 600s and S/N ranging from 120 to 243. The observations are summarized in Table 3. We looked at the radial velocities publicly available in the archive, which are derived from the cross-correlation of

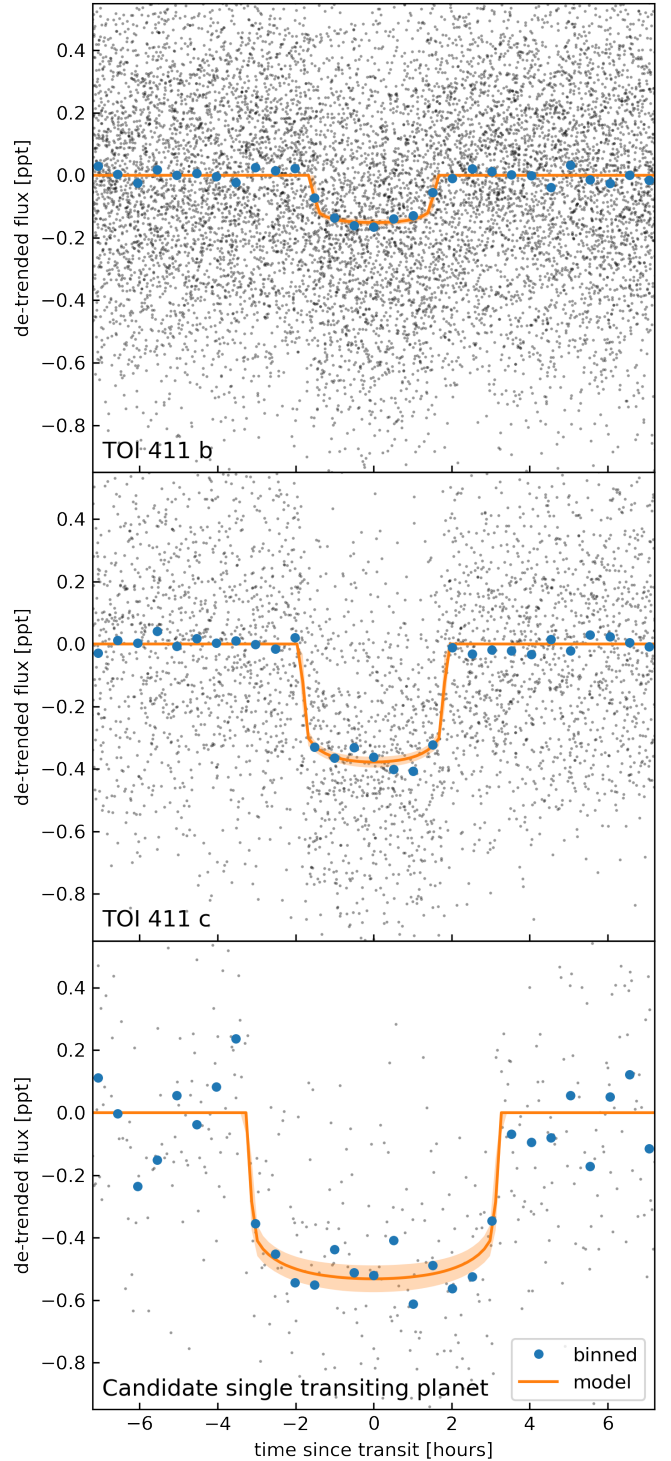


Fig. 5. Folded TESS light curves from sectors 3, 4, 30, and 31 corresponding to the transits of planet *b* (top panel), planet *c* (middle panel), and the single event transit of candidate planet *d* from sector 4 (bottom panel). The exoplanet fits of the transits are overplotted (colored lines) while blue points are binned data points.

the stellar spectra with a G2 template. The data are shown in Fig. 6.

We modeled the ESPRESSO radial-velocity (V_{rad}) data using [exoplanet \(Foreman-Mackey et al. 2017; Foreman-Mackey 2018\)](#). Specifically, we included the V_{rad} data with the transit model and performed a joint, self-consistent model. As

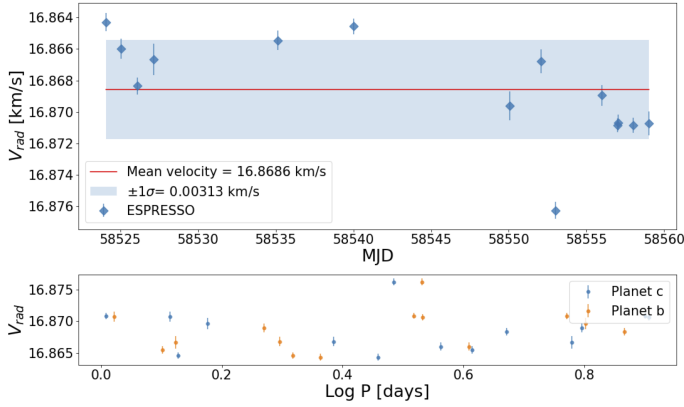


Fig. 6. *Upper panel:* ESPRESSO precise radial-velocity measurements of TOI-411 taken over February and March 2019. *Lower panel:* radial-velocity measurements have been phase-folded on the periods of planet candidates TOI-411 *b* and *c*.

Table 3. ESPRESSO radial-velocity measurements of HD 22946.

$CCF_{V_{rad}}$ (km s ⁻¹)	$CCF_{V_{rad,rr}}$ (km s ⁻¹)	$\langle S/N \rangle$	MJD
16.864287	0.000561	181	58524.05723591
16.865981	0.000627	164	58525.05175402
16.868350	0.000553	184	58526.09212435
16.866658	0.001012	109	58527.12891579
16.865454	0.000619	168	58535.12063523
16.864550	0.000496	203	58540.03340549
16.869616	0.000916	119	58550.06931525
16.866772	0.000763	139	58552.06584297
16.876263	0.000540	188	58553.01522444
16.868946	0.000662	156	58555.99860106
16.870850	0.000447	224	58557.00297657
16.870675	0.000487	208	58557.06290428
16.870844	0.000482	210	58558.02527738
16.870741	0.000766	138	58559.03833688

parts of the V_{rad} component of the model, we included a periodic Gaussian Process with a characteristic timescale of 50 days and an amplitude of 2 m s^{-1} . The values chose were selected to be longer than any Keplerian signal from the planets, and designed to encompass any long-term variations in the data. The period of planet *d* was fixed to 46 days. The posterior distributions of the semi-amplitudes are consistent with nondetection of any signal in the radial-velocity data, with 3σ upper limits of 4.1, 3.5, and 8.4 m s^{-1} for planets *b*, *c*, and *d*, respectively. These values for the semi-amplitudes yield upper mass limits of ~ 11 , 14.5, and $24.5 M_{\oplus}$. The masses are forecast to be in the region of 3.6, 8.0, and $11 M_{\oplus}$ (Chen & Kipping 2017), and therefore the non-detection of any mass signal is not unexpected. Finally, there is evidence of a slope in the V_{rad} data, although the significance is not high. In the month covered by the V_{rad} data, the star shows a 6 m s^{-1} change in measured radial velocity. This signal is consistent with an amplitude that might be seen if the source of the signal were stellar rotation or V_{rad} jitter (Luhn et al. 2020). If the source is not stellar or instrumental noise, then the slope could be due to an external body such as another planet or stellar companion. However, the available data are not sufficient to make predictions beyond saying that the data are not inconsistent with a companion more massive than Neptune on an orbital period longer than about 30 days.

4. Ruling out false positive scenarios

TESS is designed to have a large field of view ($24^{\circ} \times 96^{\circ}$) to survey 85% of the entire sky within the 2 yr of the nominal mission. As a consequence, it also has a large pixel scale ($21''$ per pixel), with a focus-limited PSF that can be as large as $1'$. This implies that the collected time-series photometry of a given target can be contaminated by nearby sources and/or unresolved background or foreground sources. Specifically, the aperture used to extract the light curve could contain more sources. The light contribution of this other source could dilute the transit signal, resulting in underestimation of the associated planetary radius. The additional source could also be an eclipsing binary of which we can only observe one set of eclipses due to signal dilution caused by the light collected from the target star producing a false positive. Therefore, the various scenarios we have to rule out include: (a) possible instrumental (systematic) effects; (b) the host star being in an eclipsing binary or multiple system; (c) the host star being close to or aligned with a foreground or background star eclipsed by a stellar companion or transited by a planet.

To exclude that the signals are due to instrumental effects, we inspected TESS Data Releases for the interested sectors to look for instrument malfunctioning and reported artifacts. As stated in Sect. 3.3, we found a feature at 2136.5 BTJD associated with one of the momentum dumps, that is, the times at which the reaction wheel speeds of the satellite are reset. We therefore decided to discard this event as an instrumental artifact. We did not find any other feature of similar nature in the entire light curve.

To clear HD 22946 from the remaining false-positive scenarios, we first directly analyzed TESS images and light curves using the DAVE pipeline (Kostov et al. 2019), as described in Sect. 4.1. Secondly, we investigated the veracity of the transit-like signals using additional ground-based time series and high-resolution imaging collected within TFOP, as described in Sects. 4.2 and 4.3. All of these tests were exclusively performed on planet candidates *b* and *c*, because they are based on the detection of multiple events and were therefore scheduled around the predictions made from the known periods. However, we note that if we assume a population of false positives randomly distributed over the entire sky, a star with at least one (confirmed) transiting planet is more likely to show signals of a second transiting planet rather than being a false positive (Latham et al. 2011; Lissauer et al. 2012; Guerrero & TESS Science Office 2021). This multiplicity factor increases the probability that a planet candidate is a true planet rather than a false positive by a factor of 20–50 (Rowe et al. 2014; Lissauer et al. 2014; Guerrero & TESS Science Office 2021). These considerations help us to increase our confidence in the planetary nature of all three candidates investigated in this work. To quantify this confidence, we computed the Bayesian probability that the signals are false positives with triceratops (Giacalone & Dressing 2020) and vespa (Morton 2015), as described in Sect. 4.4.

4.1. DAVE analysis

In order to tackle the false-positive scenarios (b) and (c), we first used the DAVE package, following the workflow of Cacciapuoti et al. (2022). We used different modules of the code, with the following rationale.

- **centroids** generates the in-transit and the two (before and after the event) out-of-transit images for each transit. It then subtracts the overall in-transit image from the overall out-of-transit image to produce a difference image. Finally, it measures the center of light for each difference image by

Table 4. Planet parameters.

Parameter	Median	+1 σ	-1 σ
Model parameters			
Star			
ρ (g cm ⁻³)	1.10	0.19	0.16
Limb darkening u_1	0.18	0.20	0.13
Limb darkening u_2	0.19	0.28	0.24
TOI-411 <i>b</i>			
T_0 (BJD-2457000)	1385.729875	0.004361	0.001199
ln Period (days)	1.396319	0.000006	0.000010
Impact parameter	0.29	0.23	0.12
Depth (ppm)	151	10	10
Eccentricity	0.126	0.190	0.009
ω (rad)	-0.7	2.2	2.9
TOI-411 <i>c</i>			
T_0 (BJD-2457000)	1386.188119	0.001278	0.001313
ln Period (days)	2.2589566	0.0000027	0.0000024
Impact parameter	0.42	0.20	0.27
Depth (ppm)	378	17	16
eccentricity	0.16	0.17	0.10
ω (rad)	0.2	2.2	2.4
Single transit event			
T_0 (BJD-2457000)	1425.164717	0.002288	0.001901
ln Period (days)	–	–	–
Impact parameter	0.35	0.21	0.23
Depth (ppm)	531	43	42
Eccentricity	–	–	–
ω (rad)	–	–	–
Derived parameters			
TOI-411 <i>b</i>			
Period (days)	4.040301	0.000023	0.000042
R_p/R_*	0.01173	0.00045	0.00045
Radius (R_\oplus)	1.48	0.06	0.06
a/R_*	9.84	0.53	0.51
a (AU)	0.0528	0.0030	0.0030
Inclination (deg)	88.3	1.1	1.2
Transit duration (h)	2.92	0.34	0.58
Equilibrium temperature (K)	1378	36	36
TOI-411 <i>c</i>			
Period (days)	9.573096	0.000026	0.000023
R_p/R_*	0.02161	0.00077	0.00075
Radius (R_\oplus)	2.74	0.14	0.14
a/R_*	17.49	0.95	0.91
a (AU)	0.0939	0.0054	0.0054
Inclination (deg)	88.57	0.86	0.53
Transit duration (h)	3.90	0.81	0.82
Equilibrium temperature (K)	1033	27	27
Single transit event			
Period (days)	–	–	–
R_p/R_*	0.0255	0.0012	.0012
Radius (R_\oplus)	3.23	0.19	0.19
a/R_*	–	–	–
a (AU)	–	–	–
Inclination (deg)	–	–	–
Transit duration (h)	6.58	1.1	1.4
Equilibrium temperature (K)	–	–	–

Notes. The priors for each fitted quantity are explained in the text (Sect. 3.4).

fitting the TESS pixel response function (PRF⁸) to the image and computes the overall photocenter by averaging over all the events examined at the previous step. The aim of this procedure is to pinpoint the true source of the transit-like events. See [Kostov et al. \(2019\)](#) for further details.

- **modelshift** phase-folds the light curve and convolves it with the best-fit trapezoid transit model, thus highlighting light-curve features. Furthermore, it shows the average of the input primary signals, the average of the odd and even signals, and the most prominent secondary, tertiary, and positive features. These results allow us to investigate the possibility that the source of the signal is an eclipsing binary. See [Kostov et al. \(2019\)](#) for further details.
- **DAVE** finally runs the **astropy**-implemented Lomb-Scargle periodogram and generates a PDF file showing both the light curve phase-folded on the period of the inspected signal and the LS period. This test is performed to check whether light-curve modulations occur on (half) the orbital period of the candidate. This is typical of beaming, reflection, and ellipsoidal effects of binary systems (see e.g., [Morris & Naftilan 1993](#); [Faigler & Mazeh 2011](#); [Shporer 2017](#)).

DAVE results for both TOI-411.01 and TOI-411.02 show no significant additional eclipse in the light curves, no odd–even differences in consecutive signals, nor flag the shapes of the transits. Even though some transits of planets *b* and *c* produce unreliable photocenter difference images due to their low S/N, the transits that are reliable confirm that the target star is the true source of the signal. For every sector, the average of all photocenters for each difference image of planets *b* and *c* falls on the target star. As no significant shift is found, HD 22946 can be considered the source of the recovered signals, at the TESS resolution limit. Regarding planet candidate *d*, no reliable photocenter measurement can be drawn due to the fact that only a single event has been observed by TESS. **Modelshift** also requires periodic signals, so it cannot be applied to the single-event candidate *d*. Several resulting images of the **centroids** module and examples of **Modelshift**'s results are shown in Figs. A.1–A.4.

Finally, it is worth mentioning that TOI-411 *b* passed all the automated SPOC pipeline data validation (DV) diagnostic tests except the difference-image centroiding test for sectors 4 and 31. However, the difference-image centroiding tests for this planet are affected by the fact that TOI-411 appears to be slightly saturated and the S/N of the transit signal is low (~ 10). TOI-411 *c* passed all the DV diagnostic tests, including the difference-image centroiding tests (except sector 4). Both transit signatures passed the odd–even transit depth tests reported by the DV. The summary of these results can be found on [ExoFOP-TESS⁹](#).

4.2. Ruling out nearby eclipsing binaries

We acquired ground-based time-series follow-up photometry of the stars in the field around TOI-411 as part of the TESS Follow-up Observing Program (TFOP; [Collins 2019](#))¹⁰. Observations were scheduled to cover the times of transit of TOI-411.01 and TOI-411.02, predicted by the initial published Quick Look Pipeline (QLP, [Huang et al. 2020](#)) ephemerides from TESS

⁸ For more information about TESS PRF see https://archive.stsci.edu/files/live/sites/mast/files/home/missions-and-data/active-missions/tess/_documents/TESS_Instrument_Handbook_v0.1.pdf

⁹ <https://exofop.ipac.caltech.edu/tess/target.php?id=100990000>

¹⁰ <https://tess.mit.edu/followup>

sectors 3 and 4 using the TESS Transit Finder, which is a customized version of the **Tapir** software package ([Jensen 2013](#)). If the events detected in the TESS data are indeed on-target, the shallow QLP-reported depths of 280 ppm and 166 ppm for TOI-411.01 and TOI-411.02, respectively, would not generally be detectable in ground-based observations. Instead, we saturated the bright star TOI-411 to enable the extraction of light curves of nearby fainter stars to attempt to rule out or identify nearby eclipsing binaries (NEBs) as potential sources of TESS detection.

We observed an ingress plus about 50% of a predicted TOI-411.01 event and a full transit of TOI-411.02 using the Las Cumbres Observatory Global Telescope (LCOGT; [Brown et al. 2013](#)) 1.0 m network nodes at the South Africa Astronomical Observatory and Cerro Tololo Inter-American Observatory, respectively. The TOI-411.01 observation was on UTC 2019 February 24 in Sloan *r'*-band and the TOI-411.02 observation was on UTC 2020 December 2 in Sloan *i'* band. The 1 m telescopes are equipped with 4096×4096 SINISTRO cameras with an image scale of $0''.389$ per pixel, resulting in a $26' \times 26'$ field of view. The images were calibrated by the standard LCOGT BANZAI pipeline ([McCully et al. 2018](#)). Photometric data were extracted using **AstroImageJ** ([Collins et al. 2017](#)).

Additionally, full transit duration observations were performed with the 0.305 m Perth Exoplanet Survey Telescope (PEST) in the *Rc* filter on the nights of 2019 February 16 (TOI-411.02) and 2020 December 06 (TOI-411.01). The data reduction and the aperture photometry were performed using a custom pipeline based on **C-Munipack**¹¹.

Although the original analyses were based on the initial published QLP ephemerides from TESS sectors 3 and 4, we reanalyzed the data relative to the TOI-411.01 and TOI-411.02 ephemerides derived in this work. We checked for possible NEBs that could be contaminating the SPOC and QLP photometric apertures, which generally extend $\sim 1'$ from the target star. To account for possible contamination from the wings of the PSFs of neighboring stars, we searched for NEBs in all known *Gaia* EDR3 and TIC version 8 nearby stars out to $2.5'$ from TOI-411 that are possibly bright enough in TESS-band to produce the TESS detection (assuming a 100% eclipse and 100% contamination of the TESS aperture). In order to account for possible delta-magnitude differences between TESS-band and the follow-up filter bands, we checked stars that are an extra 0.5 magnitudes fainter in TESS-band than needed. We consider a star cleared of an NEB if the RMS of its 10-min binned light curve is more than a factor of 5 smaller than the adjusted expected NEB depth in the star (adjusted to allow for the potential TESS-band delta-magnitude difference). We then visually inspect the light curve of each neighboring star to ensure no obvious eclipse-like signal.

The transit depths we derive in this work are deeper than the initial QLP depths. To be conservative when checking for potential NEBs, we used the shallower TOI-411.02 QLP depth of 166 ppm to calculate adjusted expected depths in all of the nearby stars. This resulted in a check of the ten stars labeled T2 through T11 in Fig. 7. To simplify the presentation of the results, we also checked the same ten stars for the deeper transit of TOI-411.01. The faintest star we checked is T2 (TIC 100990001), which has a delta-TESS-band magnitude of 9.86 according to TIC version 8. Assuming its true delta magnitude is 9.36 in the follow-up filter bands, a 92% eclipse in T2 would produce a 166 ppm depth in TOI-411. We find that the RMS of all ten light curves for each planet candidate are more than a factor of 5 smaller than the

¹¹ <http://c-munipack.sourceforge.net/>

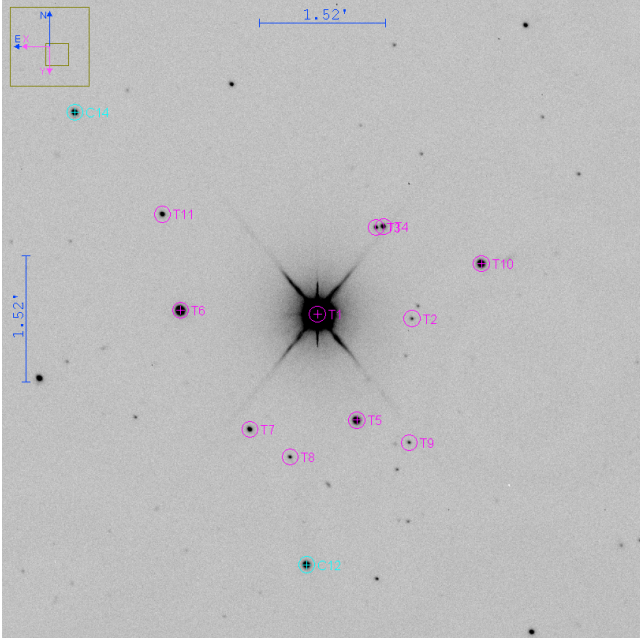


Fig. 7. Las Cumbres Observatory image of the host star HD 22946 in the *rp* filter. The ten sources identified by pink circles as T2 through T11 are within a $2.5''$ radius of TOI-411 and are potentially bright enough (see text) to cause the TOI-411 *b/c* signals. The nine closest nearby sources are also displayed in Fig. 3 and fall just outside the automatic, SPOC-based aperture used in Sector 4.

adjusted expected NEB depth in the respective star. All of our follow-up light curves and supporting results are available on the EXOFOP-TESS website¹².

Finally, we note that no observations could be carried out to perform a similar analysis for planet candidate *d*, because the orbital period is unknown and we therefore cannot make reliable predictions for the epoch of the next transits.

4.3. Ruling out unresolved stellar companions

Unresolved, dimmer stars could fall in the same $21''$ -wide TESS pixel. If an additional source is indeed present, and if this source is an eclipsing binary, its (diluted) eclipses might be the signals we observe in the light curve. In addition, the light contamination due to this unresolved star (system) might dilute the transit candidates, resulting in underestimated radii for the exoplanets (see e.g., Furlan et al. 2017; Ciardi et al. 2015). To rule out stellar companions and foreground or background stars at close separations unresolved in TESS images, we obtained speckle imaging observations with the 8 m Zorro instrument of the Gemini-South telescope (Scott et al. 2021), which provides speckle imaging simultaneously in two bands centered at 562 nm and 832 nm, resulting in reconstructed images and robust contrast limits on companion detections (see Howell et al. 2011, 2016). TOI-411 was also observed with the 4.1 m Southern Astrophysical Research (SOAR) telescope (Ziegler et al. 2020, 2021) speckle imaging camera HRCam (Tokovinin 2018). Specifically, HD 22946 was observed with Zorro on 2020 November 21 and 2020 November 25 in both bands. The estimated PSF at the time of observations was $0.02''$. The 5σ sensitivity curves and the reconstructed images for the two bands are shown in Fig. 8. We find that TOI-411 has no companion brighter than about 5 to 8 magnitudes, respectively, from about $0.1''$ out to

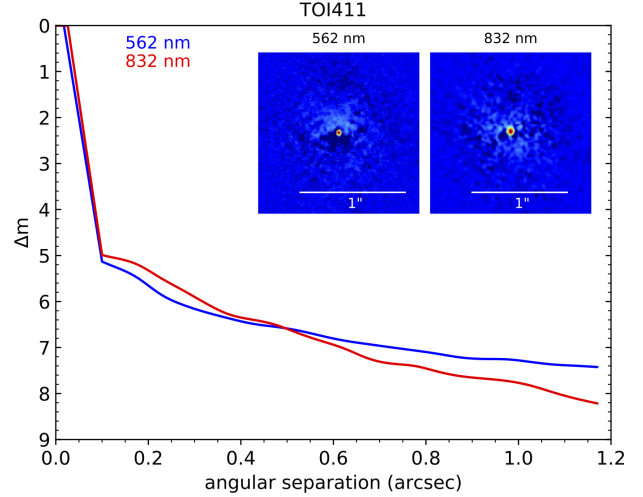


Fig. 8. Gemini-South Zorro's speckle high-contrast imaging observations of TOI-411 on UT 2020-11-25: 5σ sensitivity curves and reconstructed images. The data show that there are no close-in companions detected down to 5 mag fainter than our target at a separation of 0.1 arcsec.

$1.2''$. Observations with the HRCam on the SOAR were carried out on the UT 2019-02-18 in the *I*-band, centered at 879 nm. The estimated PSF at the epoch of the observations was $0.06''$. The auto-correlation functions for the data obtained with SOAR observations is shown in Fig. 9. No nearby star is detected within $3''$ of TOI-411, which corresponds to 188 AU at the distance of the target. Finally, we note that the host star HD 22946 was also analyzed by Kervella et al. (2019, 2022) for proper motion anomalies that could be induced by an unresolved orbiting companion, resulting in a nondetection. The *Gaia* renormalised unit weight error (RUWE) of the star is indeed 1.039 , which is a typical value for single bright stars (Gaia Collaboration 2021; Ziegler et al. 2020), thus further confirming the single-star scenario.

4.4. Quantifying the false-positive probability for different scenarios

To quantify the false-positive probability (FPP) for this system, we use the *triceratops* (Giacalone et al. 2021; Giacalone & Dressing 2020) and *vespa* (Morton 2015) packages. *triceratops* is an algorithm that rules out astrophysical false positives by calculating and comparing the probabilities of various transit-producing scenarios. *triceratops* is specifically designed for TESS observations that consider transit scenarios originating from the target star, sources unresolved with the target star, and known nearby stars within 2.5 arcmin from the target star. This tool encapsulates the total probability that a planet candidate is a false positive in the false-positive probability (FPP) and the probability that the planet candidate is a false positive originating from a known nearby star in the nearby false-positive probability (NFPP). For a planet candidate to be validated, it must achieve $FPP < 0.01$ and $NFPP < 0.001$ (see Giacalone et al. 2021, for more details). As an additional constraint in our calculations, we fold in the speckle imaging follow-up observations discussed in the previous section. Because these observations reveal no previously unresolved companions within their detection limits, incorporating the follow-up reduces the calculated probability of the transit originating from a bound or chance-aligned star within the resolution limits of the target star, thereby reducing the FPP of the planet candidate. We note that, as the true period of planet *d* is unknown, we cannot perform this kind of analysis for it.

¹² <https://exofop.ipac.caltech.edu/tess>

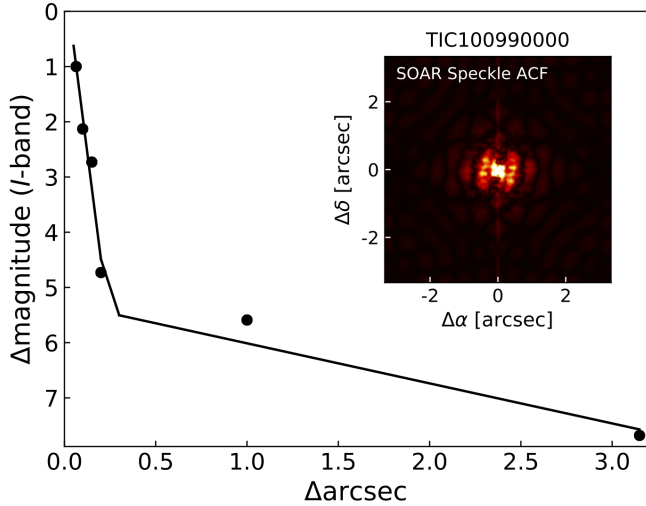


Fig. 9. Analysis of the SOARCam high-contrast image of TOI-411: the two-dimensional autocorrelation function and the reconstructed image of the field are shown. The data show that there are no close-in companions detected within 3 arcsec of TOI-411, which would show up as additional peaks in the autocorrelation function.

Otherwise, we ran *triceratops* 20 times for each of the planet candidates *b* and *c* and calculated the mean and standard deviation of the resulting FPPs and NFPPs. We found $FPP = (0.88 \pm 1.28) \times 10^{-7}$ and $FPP = (3.56 \pm 1.27) \times 10^{-4}$ for TOI-411.01 and TOI-411.02, respectively. Because *triceratops* determines that no nearby stars are capable of being sources of astrophysical false positives, we find $NFPP = 0$ for both candidates. Based on these results, we consider planets *b* and *c* to be validated.

Additionally, we used *vespa* to independently validate the same signals. *vespa* compares transit signals to a number of false-positive scenarios including an unblended eclipsing binary (EB), a blended background EB, a hierarchical companion EB, and the “double-period” EB scenario. It accounts for the period, depth, duration, and shape of each signal, as well as the colors of the target star, spectroscopic and imaging follow-up observations, and simulations of the population and distribution of field stars and binary stars at the position of the target. We ran *vespa* on the TESS light curves to calculate the FPP for each individual planetary signal after masking additional potential transits for each target signal. The observational constraints derived from the high-contrast imaging of TOI-411 by Gemini-South Zorro were included in this case as well. *vespa* is particularly sensitive to the constraint on the maximum depth of potential secondary eclipses and the maximum radius at which *vespa* considers the influence of background binary systems. We used the *DAVE* analysis to estimate the secondary depth constraint and set the maximum radius parameter at $21''$ to emulate the size of a TESS pixel. Using these inputs, we calculated an FPP of 7.77×10^{-12} and 4.51×10^{-5} for TOI-411.01 and TOI-411.02, respectively. These values are well below the commonly suggested 0.01 threshold required to statistically validate these candidates as planets, in agreement with the results from *triceratops*.

5. The HD 22946 planetary system

In this section, we present the main properties of the planetary system orbiting HD 22946. The three planets are a $1.48 \pm 0.06 R_{\oplus}$ super-Earth (planet *b*), and $2.35 \pm 0.08 R_{\oplus}$ (planet *c*) and a

$2.78 \pm 0.13 R_{\oplus}$ (planet *d*) sub-Neptunes. In Sect. 5.1, we estimate the planet masses and the expected semi-amplitudes of radial-velocity curves that could be measured.

In Sect. 5.3, we perform N-body simulations to assess the dynamical stability of the system, while in Sect. 5.4 we investigate the dynamical packing of the system to determine whether additional planets might be orbiting HD 22956. Finally, we evaluate the capability of spectroscopic follow-ups with the JWST NIRISS instrument in Sect. 5.5 for the detection of possible atmospheres.

5.1. Planet mass estimates

While TOI-411 has been observed with ESPRESSO and a total of 14 radial-velocity measurements are available as explained in Sect. 3.4, we note that a significantly larger number of spectra would be needed to place meaningful mass constraints on the planets of the TOI-411 system. Given the lack of them, we use empirical radius–mass relations to estimate the masses of these planets.

We make use of two different equations for the inner planet and the outer ones. In fact, while the well-known [Chen & Kipping \(2017\)](#) relations have been widely used in the literature to estimate the masses of exoplanets of any size, [Otegi et al. \(2020\)](#) showed that a slightly different equation better constrains super-Earths ($1.5 < R/R_{\oplus} < 2$). Thus, adopting the planet radii in Table 4 and using [Chen & Kipping \(2017\)](#) relations, we estimate the masses of planets *c* and *d* to be $M_c = 6.03 \pm 0.037 M_{\oplus}$ and $M_d = 8.01 \pm 0.68 M_{\oplus}$, respectively. On the other hand, considering the corrections of [Otegi et al. \(2020\)](#), we estimate a mass of $M_b = 3.49 \pm 0.52 M_{\oplus}$ for planet *b*.

Given the brightness of the host star ($V \approx 8.3$ mag), these planets are optimal targets for mass measurements by means of radial-velocity curves. In fact, the computed mean masses yield V_{rad} semi-amplitudes of 1.31 ± 0.19 m/s, 1.70 ± 0.10 m/s, and 1.33 ± 0.12 m/s, respectively, which are well within the capabilities of current Southern Hemisphere instruments such as HARPS ([Pepe et al. 2002](#)) and ESPRESSO ([Pepe et al. 2014](#)), assuming an intensive monitoring.

5.2. Transit timing variation analysis

In order to obtain independent estimates of the planetary masses, we performed a transit timing variation (TTVs) analysis, which is also able to find possible undetected planets. We modeled the TOI-411 system with the TRANSITFIT5 transit modeling software ([Rowe & Thompson 2015](#); [Rowe 2016](#)). We computed a multi-planet fit that includes all three planets and assumes non-interacting Keplerian orbits. The best-fit model was then used to create a theoretical light curve with two of the other planets removed, thus isolating a single planet. The single-planet light curve was then used to measure the center of the transit times for each transit event. We did not find any obvious sign of TTV. The period ratio of planets *b* and *c* is not close to strong orbital resonance and the potentially long period of *d* suggests all three planets are not strongly dynamically coupled.

5.3. Dynamical stability

In order to validate the derived planetary architecture of the system, we performed a set of dynamical simulations to investigate the dynamical integrity of the orbits and possible eccentricity variations induced by the proximity of the planets to each other. We performed one simulation including only planets *b* and *c*, and a set of different simulations on a range of possible values for

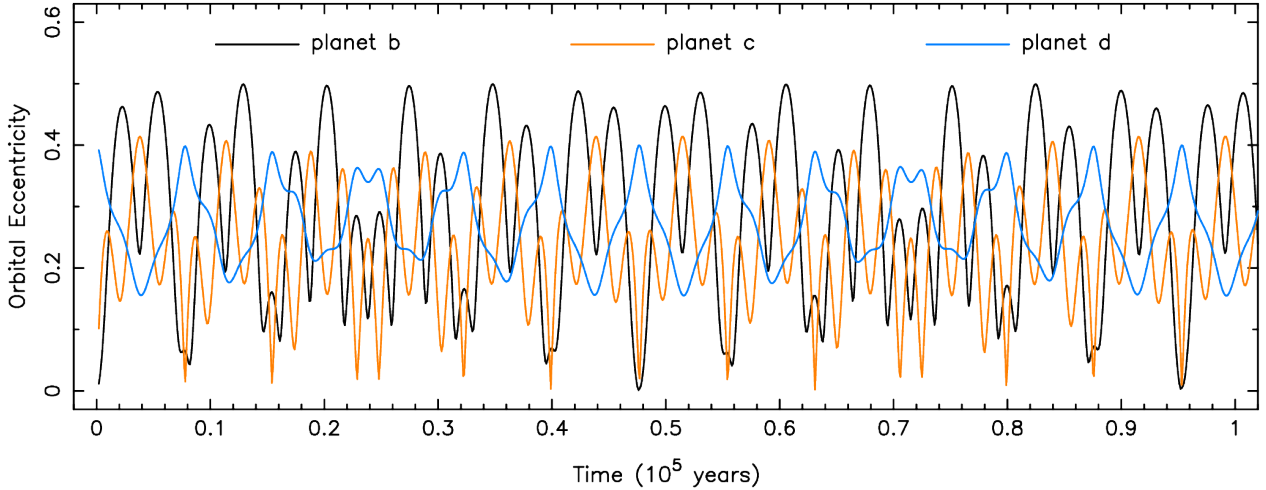


Fig. 10. One of the simulated eccentricity evolutions of the HD 22946 system over 10^5 yr. In the case shown here, we assume the following extreme initial conditions for planet *d*: initial semi-major axis of 0.19 AU and eccentricity of 0.4.

the semi-major axes of planet *d*, given its uncertain location. We adopted the stellar parameters shown in Table 2 and the planetary properties provided by Table 4.

All simulations were carried out using the *N*-body integration capabilities of the Mercury Integrator Package (Chambers 1999) and adopting a methodology similar to the one described by Kane & Raymond (2014) and Kane (2016). They were carried out on a hybrid symplectic/Bulirsch-Stoer integrator with a Jacobi coordinate system (Wisdom & Holman 1991; Wisdom 2006), with a time resolution of 0.2 days to ensure adequate sampling of the planetary orbits, on a time span of 10^7 yr. Results from the simulation of planets *b* and *c* alone show that they are in exceptionally stable orbits that remain approximately circular, inferring minimal dynamical interactions between them.

To study the effects of planet *d*, we assumed a value for the semi-major axes in the range from 0.19 to 0.26 AU, corresponding to the mean and -1σ values for the constrained period of 46 ± 4 days. We only considered the -1σ (and not the $+1\sigma$) scenario to put ourselves in the most dynamically extreme situation for which the planet orbits as close as possible (within our predictions) to the other two celestial bodies and its gravitational influence has a larger effect. The system remained stable through the semi-major axis range for planet *d* and for the full duration of the simulations. We further investigated the effects of high eccentricities for planet *d* and found that eccentricities as high as 0.4 still allow for fully stable orbits within the system even in the most compact configuration.

For example, Fig. 10 shows the eccentricity evolution of the three planets for the extreme scenario where planet *d* is located in a 0.19 AU orbit with a starting eccentricity of 0.4. Remarkably, the stability of the system enables a seamless transfer of angular momentum between the planets in long-term sustainable cycles. These results show that the HD 22946 planetary system is dynamically sustainable, strengthening the self-consistency of our analysis.

5.4. Possible undetected planets

Here, we investigate the presence of potentially undetected planets orbiting in the gaps between the planets presented in this work following the same approach as that of Humphrey & Quintana (2020). Gladman (1993) defined a system of two planets as

Hill-stable (unstable) if the separation between the two, Δ , normalized by the mutual Hill-radius (R_H) of the pair is above (below) an analytically defined critical level, Δ_{crit} . In the more general case of multi-planetary systems, Chambers et al. (1996); Pu & Wu (2015) used numerical simulations to retrieve the minimum value of Δ_{crit} above which the pair can be considered dynamically stable. Chambers et al. (1996) simulated systems with circular, coplanar orbits, and found that a $\Delta_{\text{crit}} = 10$ can be generally used to measure the stability of multi-planet systems within the described prescriptions. Pu & Wu (2015) found the same Δ_{crit} as Chambers et al. (1996) for systems on circular and coplanar orbits but extended their simulations by including system eccentricities and inclinations drawn from a Rayleigh distribution. These latter authors find that planet pairs with $\Delta < \Delta_{\text{crit}} = 12.3$ are expected to experience close encounters, orbit crossing events, and/or ejections due to strong gravitational interaction between the planets. Considering these two values for Δ_{crit} , we can verify whether or not the HD 22946 system could host, between each planet pair, an additional planet without jeopardizing the system stability. Following Humphrey & Quintana (2020), we computed the interval ($[a_{x\text{min}}, a_{x\text{max}}]$) of possible semi-major axes for a potential additional planet in a range of possible masses M_x for both the *b/c* and the *c/d* pair. If, for a given mass, $a_{x\text{min}} \leq a_{x\text{max}}$, the planet pair is considered unpacked, that is, there is enough space to host an additional planet that would not destabilize the system. By solving Eqs. (2) and (3) of Humphrey & Quintana (2020), one can compute ($M_{x\text{max}}, a_x$), the maximum mass that a potential undetected planet could have without destabilizing the system and its related semi-major axis. We computed $a_{x\text{min}}$ and $a_{x\text{max}}$ for each value of Δ_{crit} for both couples in the system. The results are shown in Fig. 11. Both planet pairs are unpacked for each value of Δ_{crit} , though there is quite limited space for an additional planet between TOI-411 *b* and *c*. The planets TOI-411 *c* and *d*, on the other hand, might host an additional planet as large as $0.4 M_J$ based on the least stringent Δ_{crit} value of 10. Table 5 shows the computed values for $M_{x\text{max}}$ and related a_x under the two different Δ_{crit} conditions. We searched the light curve with the TLS pipeline in the intermediate range of periods and found no evidence for additional transiting candidates. However, there is the possibility that a potentially undetected planet is not observed transiting the star due to its orbital inclination and

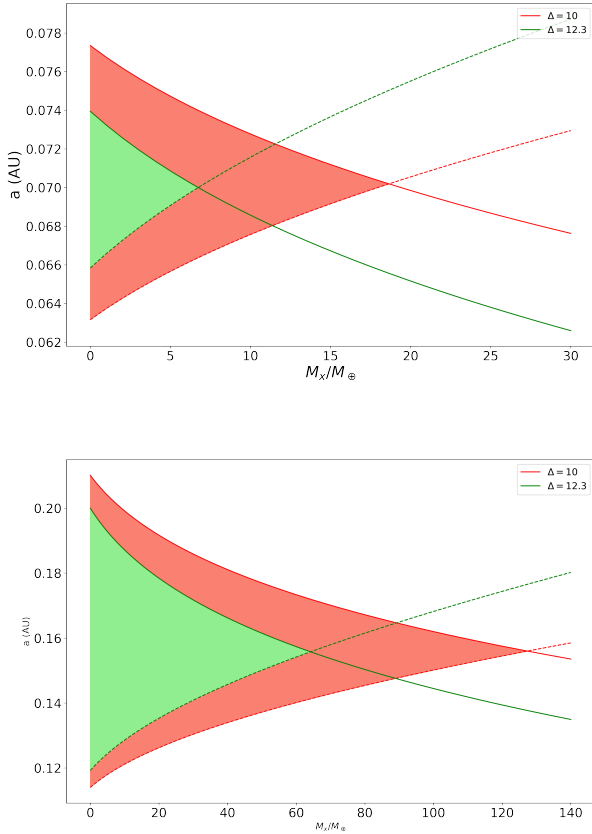


Fig. 11. Mass and semi-major axis of a possible undetected planet between TOI-411 *b/c* (upper panel) and TOI-411 *c/d* (lower panel). The minimum semi-major axis ($a_{x\min}$) is shown as a dashed line and the maximum one ($a_{x\max}$) is shown as a continuous line for $\Delta_{\text{crit}} = 10$ and 12.3 in red and green, respectively. Given Δ_{crit} , the shaded region contains the possible combinations (M_x, a_x) for a stable system configuration hosting one more planet.

Table 5. Maximum mass $M_{x\max}$ and related semi-major axis a_x of a potential additional planet orbiting between planets *b/c* or *c/d*.

Pair <i>b/c</i>	$M_{x\max}/M_{\oplus}$	a_x (AU)
$\Delta_{\text{crit}} = 10$	18.6	0.0698
$\Delta_{\text{crit}} = 12.3$	6.7	0.0693
Pair <i>c/d</i>	$M_{x\max}/M_{\oplus}$	a_x (AU)
$\Delta_{\text{crit}} = 10$	127.4	0.156
$\Delta_{\text{crit}} = 12.3$	64.2	0.156

Notes. Two different values for Δ_{crit} are considered (see text).

might be discovered via precise radial-velocity techniques such as those described by Demangeon et al. (2021).

5.5. Potential for atmospheric characterization

The observed period and derived radius for TOI-411 *b* place it in the range of hot super-Earths; specifically, in the $1.5\text{--}2.0 R_{\oplus}$ interval where a scarcity of exoplanets has been observed by Fulton et al. (2017). This is considered to be a transition region from rocky worlds with a high-molecular-weight atmosphere, to low-density worlds dominated by a H/He gaseous envelope. The former may have accreted a primary atmosphere in the early stages of formation that might have been dispersed due to escape

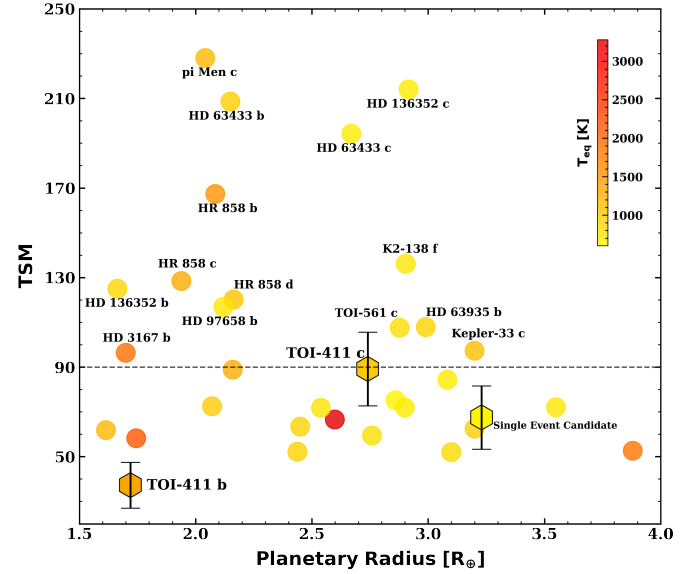


Fig. 12. Transmission spectroscopy metric values for known exoplanets orbiting F/G stars in less than 50 days. We only show exoplanets for which $\text{TSM} > 50$ for clarity as $\sim 98\%$ of worlds in the sample lay below this value. While TOI-411 *b* and *c* fall in the 2% of this kind of planet with $\text{TSM} > 50$, only TOI-411 *c* passes the suggested threshold of 90, joining an elite group of 15 super-Earths and sub-Neptunes orbiting Sun-like stars and amenable for spectroscopic follow-up with JWST.

processes, such as stellar radiation photo-evaporation (Fulton & Petigura 2018) or core-powered mass loss (Ginzburg et al. 2018). The only super-Earth with a detected (and largely discussed) atmosphere is 55 Cnc *e*, which probably lost its primary H/He envelope (Zhang et al. 2021). Even if TOI-411 *b* did lose its primary atmosphere during early evolution, a large reserve of hydrogen could still be trapped in its mantle (Kite et al. 2019). This could lead to the out-gassing of a secondary atmosphere, as suggested in the case of the Earth-like planet GJ 1132 *b* (Swain et al. 2021). Precise radial-velocity measurements and improved mass estimates will be critical to determining the mean density of the planet and constraining its composition. TOI-411 *c* and the single transit event candidate appear to be a hot and a warm sub-Neptune, respectively, and therefore they could potentially hold a thick H/He envelope. Future observations with new generation telescopes of these $< 4 R_{\oplus}$ exoplanets will be crucial for identifying their atmospheric composition and narrowing down the possibilities regarding their formation mechanisms. For this purpose, following the methods of Kempton et al. (2018), we estimated the potential for atmospheric follow-up of these worlds with the *James Webb* Space Telescope (JWST). We computed the transmission spectroscopy metric (TSM), a quantity proportional to the expected S/N of the transmission spectrum of a cloud-free atmosphere, over a 10-h observation in the NIRISS bandpass. The TSM values for planets *b* and *c* and candidate *d* are, respectively, 65 ± 10 , 89 ± 16 , and 67 ± 14 . We note that the TSM value is intended as a rough indicator for transmission spectroscopy follow-ups that can and should be refined with precise mass measurement of the planets. We put our planets into context by comparing their TSM with the same quantity for similar worlds. Specifically, Fig. 12 shows the TSM values for every confirmed planet listed on the NASA Exoplanet Archive¹³ orbiting F/G stars, with $1.5 R_{\oplus} < R_p < 4.0 R_{\oplus}$ and

¹³ <https://exoplanetarchive.ipac.caltech.edu/index.html>

$P_{\text{orb}} < 50$ days. The lower limit is chosen to discard the terrestrial planets for which the [Kempton et al. \(2018\)](#) TSM threshold is set to 10 whilst the upper limit keeps the sample within the sub-Neptune radius range. The reported equilibrium temperature (T_{eq}) was computed for each planet by assuming null albedo and full day–night heat redistribution. Within this sample of 1140 planets, only 1.2% of them have a TSM value above the threshold of 90 that [Kempton et al. \(2018\)](#) indicates to qualify the planet as suitable for atmospheric detection with JWST, and TOI-411 *c* can potentially overcome this threshold.

6. Conclusions

We present the discovery of a multi-planetary system around the bright ($V \sim 8.3$ mag), nearby (~ 63 pc) Sun-like star HD 22946, indicated also as TOI-411 from TESS data. The host star was observed by TESS in Sectors 3, 4, 30, and 31 and two transiting planets with periods of 4.04 and 9.57 days were identified in the light curve, with an additional single event that we associate to a third transiting planet with a period of 46 ± 4 days. By modeling the transits, we determine the planet radii: $1.48 \pm 0.06 R_{\oplus}$ for planet *b*, $2.35 \pm 0.08 R_{\oplus}$ for planet *c*, and $2.78 \pm 0.13 R_{\oplus}$ for planet *d*.

While the nature of the single event cannot be verified using exclusively TESS data, and follow-ups are not yet available, we vetted the innermost exoplanets, considering several different aspects: we used the pipelines **DAVE**, **vespa**, and **triceratops** to exclude false-positive scenarios or determine that the false-positive probability is negligible, whilst we used TFOP photometric data and high-resolution imaging to rule out faint bound companions and foreground, background, or nearby eclipsing binaries that could contaminate the TESS light curve. Therefore, we validate the discovery of planets *b* (or TOI-411.02) and *c* (or TOI-411.01), while we plan to collect additional data (radial-velocity curve and photometric follow-up observations) in order to further confirm the nature of candidate planet *d* (or TOI-411.03)

Multi-planetary systems around Sun-like stars, such as the one reported here, are ideal laboratories for testing our understanding of how planets form and evolve. TOI-411 *b*, with an inferred mass of $\sim 3.5 M_{\oplus}$, is a hot super-Earth ([Fulton et al. 2017](#); [Fressin et al. 2013](#)) orbiting its star with a period of ≈ 4 days at the equilibrium temperature of 1378 ± 36 K. Because of its size, it is one of the relatively few planets found within the Fulton gap, that is, a range of planetary radii of between 1.5 and $2 R_{\oplus}$ that is relatively less populated ([Fulton et al. 2017](#)) with respect to smaller or larger radii. This bimodality in the distribution of the planets is thought to be the effect of photoevaporation of volatile gases or core-powered mass loss that strips low-mass planets of their atmosphere, leaving behind bare, rocky planets, while gas giants with radii larger than $2 R_{\oplus}$ remain unaffected.

Indeed, TOI-411 *c* and TOI-411 *d* have larger radii, with a radius ratio of 1.6 and 1.8 respectively. By adopting the approach described in [Humphrey & Quintana \(2020\)](#), we find that between planet *b* and *c* it would be possible to include at least one other planet without compromising the dynamical stability of the system. In the scenario described above, this undetected planet would have an intermediate period and a smaller radius ratio. However, we do not find evidence for this intermediate planet from the TESS light curve.

With an equilibrium temperature of about 1000 K, planet *c* is a hot sub-Neptunian, and holds particular interest because it can potentially host a tick atmosphere and has a TSM compatible

with atmospheric detection from JWST. Furthermore, even if the host star is bright, its luminosity (~ 7.3 mag in the *J*-band) is still below the saturation limit for the NIRISS single-object spectroscopy mode. An independent constraint on the mass value for this planet from radial-velocity measurement is critical in order to confirm the suitability of this target for atmospheric detection. On the other side, being a cold ($T_{\text{eq}} = 622$ K) sub-Neptunian, if observable, planet *d* would provide an opportunity to carry out comparative atmospheric characterization via transmission spectroscopy. In this case, the TSM estimate should be recomputed when the validation is confirmed and the period is known with better precision.

In summary, by hosting a star that is bright and similar to our Sun, and three planets with a common origin but completely different aspects, the HD 22946 multiplanetary system offers many interesting insights into planetary formation. We conclude that HD 22946 hosts one small planet stripped of its atmosphere (or with a secondary, accreted atmosphere), two larger planets at significantly different temperatures, and probably yet-to-be-discovered intermediate ones.

This system therefore provides an exciting opportunity for a synergy of space- and ground-based facilities such as the Characterising Exoplanets Satellite (CHEOPS [Broeg et al. 2013](#)), HARPS, and ESPRESSO to determine the bulk density of the planets, and possibly also for JWST to investigate the presence of an atmosphere around TOI-411 *c*. These efforts will help us to gain a better understanding of the formation pathways that can lead to a similar system.

Acknowledgements. We thank the referee for her/his comments that helped to improve and clarify the presentation of our results. This paper includes data collected by the TESS mission, which are publicly available from the Mikulski Archive for Space Telescopes (MAST). Funding for the TESS mission is provided by NASA’s Science Mission Directorate. We acknowledge the use of public TESS Alert data from pipelines at the TESS Science Office and at the TESS Science Processing Operations Center. This research has made use of the Exoplanet Follow-up Observation Program website, which is operated by the California Institute of Technology, under contract with the National Aeronautics and Space Administration under the Exoplanet Exploration Program. Resources supporting this work were provided by the NASA High-End Computing (HEC) Program through the NASA Advanced Supercomputing (NAS) Division at Ames Research Center for the production of the SPOC data products. L.I. acknowledges the “PON Ricerca e Innovazione: Attraction and International Mobility (AIM)” program for support. This work has made use of data from the European Space Agency (ESA) mission *Gaia* (<https://www.cosmos.esa.int/gaia>), processed by the *Gaia* Data Processing and Analysis Consortium (DPAC, <https://www.cosmos.esa.int/web/gaia/dpac/consortium>). Observations in the paper made use of the High-Resolution Imaging instrument Zorro at Gemini-South. The data underlying this article is publicly available at the following archives: MAST (<https://archive.stsci.edu/missions-and-data/tess>) and ExoFOP-TESS (<https://exofop.ipac.caltech.edu/tess/>). This work is based on data collected at the following facilities: ASAS-SN, Exoplanet Archive, *Gaia*, Gemini: South (Zorro), MAST, LCOGT, SOAR (HRcam), TESS. This work makes use of the following software: astropy, lightkurve ([Lightkurve Collaboration 2018](#)), transitleastsquares ([Hippke & Heller 2019](#)), DAVE ([Kostov et al. 2019](#)), exoplanet ([Foreman-Mackey et al. 2017](#); [Foreman-Mackey 2018](#)), vespa ([Morton 2015](#)), triceratops ([Giacalone & Dressing 2020](#)), tpfplotter ([Aller et al. 2020](#)).

References

- Aller, A., Lillo-Box, J., Jones, D., Miranda, L. F., & Barceló Forteza, S. 2020, *A&A*, **635**, A128
 Bitsch, B. 2019, *A&A*, **630**, A51
 Broeg, C., Fortier, A., Ehrenreich, D., et al. 2013, in *European Physical Journal Web of Conferences*, **47**, 03005
 Brown, T. M., Baliber, N., Bianco, F. B., et al. 2013, *PASP*, **125**, 1031
 Buchhave, L. A., Latham, D. W., Johansen, A., et al. 2012, *Nature*, **486**, 375
 Cacciapuoti, L., Kostov, V. B., Kuchner, M., et al. 2022, *MNRAS*, **513**, 102
 Chambers, J. E. 1999, *MNRAS*, **304**, 793
 Chambers, J. E., Wetherill, G., & Boss, A. 1996, *Icarus*, **119**, 261

- Chen, J. E., & Kipping, D. 2017, *ApJ*, **834**, 17
- Ciardi, D. R., Beichman, C. A., Horch, E. P., & Howell, S. B. 2015, *ApJ*, **805**, 16
- Collins, K. 2019, in *American Astronomical Society Meeting Abstracts*, 233, 140.05
- Collins, K. A., Kielkopf, J. F., Stassun, K. G., & Hessman, F. V. 2017, *AJ*, **153**, 77
- Cutri, R. M., Skrutskie, M. F., van Dyk, S., et al. 2003, *VizieR Online Data Catalog*: II/246
- Demangeon, O. D. S., Zapatero Osorio, M. R., Alibert, Y., et al. 2021, *A&A*, **653**, A41
- Donati, J.-F., Semel, M., Carter, B. D., Rees, D. E., & Collier Cameron, A. 1997, *MNRAS*, **291**, 658
- Eisner, N. L., Barragán, O., Lintott, C., et al. 2021, *MNRAS*, **501**, 4669
- Fabrycky, D. C., Lissauer, J. J., Ragozzine, D., et al. 2014, *ApJ*, **790**, 146
- Faigler, S., & Mazeh, T. 2011, *MNRAS*, **415**, 3921
- Foreman-Mackey, D. 2018, *RNAAS*, **2**, 31
- Foreman-Mackey, D., Agol, E., Ambikasaran, S., & Angus, R. 2017, *AJ*, **154**, 220
- Foreman-Mackey, D., Luger, R., Agol, E., et al. 2021, *J. Open Source Softw.*, **6**, 3285
- Fressin, F., Torres, G., Charbonneau, D., et al. 2013, *ApJ*, **766**, 81
- Fulton, B. J., & Petigura, E. A. 2018, *AJ*, **156**, 264
- Fulton, B. J., Petigura, E. A., Howard, A. W., et al. 2017, *AJ*, **154**, 109
- Furlan, E., Ciardi, D. R., Everett, M. E., et al. 2017, *AJ*, **153**, 71
- Gaia Collaboration (Brown, A. G. A., et al.) 2018, *A&A*, **616**, A1
- Gaia Collaboration (Brown, A. G. A., et al.) 2021, *A&A*, **650**, A3
- Giacalone, S., & Dressing, C. D. 2020, *Astrophysics Source Code Library* [[record ascl:2002.004](#)]
- Giacalone, S., Dressing, C. D., Jensen, E. L. N., et al. 2021, *AJ*, **161**, 24
- Gillon, M., Triaud, A. H. M. J., Demory, B.-O., et al. 2017, *Nature*, **542**, 456
- Ginzburg, S., Schlichting, H. E., & Sari, R. 2018, *MNRAS*, **476**, 759
- Girardi, L., Bressan, A., Bertelli, G., & Chiosi, C. 2000, *A&As*, **141**, 371
- Gladman, B. 1993, *Icarus*, **106**, 247
- Guerrero, N., & TESS Science Office. 2021, in *American Astronomical Society Meeting Abstracts*, 53, 117.01
- Hippke, M., & Heller, R. 2019, *A&A*, **623**, A39
- Hoffman, M. D., & Gelman, A. 2014, *J. Mach. Learn. Res.*, **15**, 1593
- Hog, E., Bastian, U., Egret, D., et al. 1997, *The Hipparcos and Tycho Catalogues, Astrometric and Photometric Star Catalogues Derived from the ESA HIPPARCOS Space Astrometry Mission (ESA Space Agency)*
- Howell, S. B., Everett, M. E., Sherry, W., Horch, E., & Ciardi, D. R. 2011, *AJ*, **142**, 19
- Howell, S. B., Everett, M. E., Horch, E. P., et al. 2016, *ApJ*, **829**, L2
- Huang, C. X., Vanderburg, A., Pál, A., et al. 2020, *RNAAS*, **4**, 204
- Humphrey, A. L. T., & Quintana, E. V. 2020, *ApJ*, submitted [[arXiv:2011.03053](#)]
- Jayasinghe, T., Kochanek, C. S., Stanek, K. Z., et al. 2021, *MNRAS*, **503**, 200
- Jenkins, J. M., Twicken, J. D., McCauliff, S., et al. 2016, *SPIE Conf. Ser.*, **9913**, 99133E
- Jensen, E. 2013, *Tapir: A web interface for transit/eclipse observability, Astrophysics Source Code Library* [[record ascl:1306.007](#)]
- Kane, S. R. 2016, *ApJ*, **830**, 105
- Kane, S. R., & Raymond, S. N. 2014, *ApJ*, **784**, 104
- Kempton, E. M. R., Bean, J. L., Louie, D. R., et al. 2018, *PASP*, **130**, 114401
- Kervella, P., Thévenin, F., Di Folco, E., & Ségransan, D. 2004, *A&A*, **426**, 297
- Kervella, P., Arenou, F., Mignard, F., & Thévenin, F. 2019, *A&A*, **623**, A72
- Kervella, P., Arenou, F., & Thévenin, F. 2022, *A&A*, **657**, A7
- Kipping, D. M. 2013, *MNRAS*, **435**, 2152
- Kite, E. S., Fegley Jr, B., Schaefer, L., & Ford, E. B. 2019, *ApJ*, **887**, L33
- Kostov, V. B., Mullally, S. E., Quintana, E. V., et al. 2019, *AJ*, **157**, 124
- Kovács, G., Zucker, S., & Mazeh, T. 2002, *A&A*, **391**, 369
- Latham, D. W., Rowe, J. F., Quinn, S. N., et al. 2011, *ApJ*, **732**, L24
- Li, J., Tenenbaum, P., Twicken, J. D., et al. 2019, *PASP*, **131**, 024506
- Lightkurve Collaboration (Cardoso, J. V. d. M., et al.) 2018, *Astrophysics Source Code Library* [[record ascl:1812.013](#)]
- Lissauer, J. J., Ragozzine, D., Fabrycky, D. C., et al. 2011, *ApJS*, **197**, 8
- Lissauer, J. J., Marcy, G. W., Rowe, J. F., et al. 2012, *ApJ*, **750**, 112
- Lissauer, J. J., Marcy, G. W., Bryson, S. T., et al. 2014, *ApJ*, **784**, 44
- Lomb, N. R. 1976, *Ap&SS*, **39**, 447
- Lloyd, R. O. P., Shkolnik, E. L., Schneider, A. C., et al. 2020, *ApJ*, **890**, 23
- Luger, R., Agol, E., Foreman-Mackey, D., et al. 2019, *AJ*, **157**, 64
- Luhn, J. K., Wright, J. T., Howard, A. W., & Isaacson, H. 2020, *AJ*, **159**, 235
- Mamajek, E. E., & Hillenbrand, L. A. 2008, *ApJ*, **687**, 1264
- McCully, C., Volgenau, N. H., Harbeck, D.-R., et al. 2018, *SPIE Conf. Ser.*, **10707**, 107070K
- Mermilliod, J. C. 2006, *VizieR Online Data Catalog*: II/168
- Miret-Roig, N., Bouy, H., Raymond, S. N., et al. 2022, *Nature Astronomy*, **6**, 89
- Morris, S. L., & Naftilan, S. A. 1993, *ApJ*, **419**, 344
- Morris, R. L., Twicken, J. D., Smith, J. C., et al. 2020, *Kepler Data Processing Handbook: Photometric Analysis, Kepler Science Document KSCI-19081-003*, ed. J. M. Jenkins
- Morton, T. D. 2015, *Astrophysics Source Code Library* [[record ascl:1503.011](#)]
- Murgas, F., Jenkins, J. S., Rojo, P., Jones, H. R. A., & Pinfield, D. J. 2013, *A&A*, **552**, A27
- Naef, D., Latham, D. W., Mayor, M., et al. 2001, *A&A*, **375**, L27
- Otegi, J. F., Bouchy, F., & Helled, R. 2020, *A&A*, **634**, A43
- Owen, J. E., & Wu, Y. 2017, *ApJ*, **847**, 29
- Paredes, L. A., Henry, T. J., Quinn, S. N., et al. 2021, *AJ*, **162**, 176
- Pepe, F., Mayor, M., Rupprecht, G., et al. 2002, *The Messenger*, **110**, 9
- Pepe, F., Molaro, P., Cristiani, S., et al. 2014, *Astron. Nachr.*, **335**, 8
- Percy, J. R., Au-Yong, K., Gilmour-Taylor, G., et al. 2002, in *ASP Conf. Ser.*, **256**, 99
- Petigura, E. A., Howard, A. W., Marcy, G. W., et al. 2017, *AJ*, **154**, 107
- Pojmanski, G. 1997, *Acta Astron.*, **47**, 467
- Pribulla, T., Sebastian, D., Ammler-von Eiff, M., et al. 2014, *MNRAS*, **443**, 2815
- Pu, B., & Wu, Y. 2015, *ApJ*, **807**, 44
- Ragozzine, D., & Holman, M. J. 2010, *arXiv e-prints* [[arXiv:1006.3727](#)]
- Richards, J. W., Starr, D. L., Miller, A. A., et al. 2012, *ApJS*, **203**, 32
- Ricker, G. R., Winn, J. N., Vanderspek, R., et al. 2015, *JATIS*, **1**, 014003
- Rodríguez, J. E., Quinn, S. N., Zhou, G., et al. 2021, *AJ*, **161**, 194
- Rowe, J. F. 2016, *Kepler: Kepler Transit Model Codebase Release*
- Rowe, J. F., & Thompson, S. E. 2015, *arXiv e-prints* [[arXiv:1504.00707](#)]
- Rowe, J. F., Bryson, S. T., Marcy, G. W., et al. 2014, *ApJ*, **784**, 45
- Salvatiere, J., Wiecki, T. V., & Fannesbeck, C. 2016, *PeerJ Comput. Sci.*, **2**, e55
- Scargle, J. D. 1982, *ApJ*, **263**, 835
- Schlegel, D. J., Finkbeiner, D. P., & Davis, M. 1998, *ApJ*, **500**, 525
- Scott, N. J., Howell, S. B., Gnilka, C. L., et al. 2021, *Front. Astron. Space Sci.*, **8**, 138
- Seager, S., & Mallén-Ornelas, G. 2003, *ApJ*, **585**, 1038
- Shappee, B. J., Prieto, J. L., Grupe, D., et al. 2014, *ApJ*, **788**, 48
- Shporer, A. 2017, *PASP*, **129**, 072001
- Siverd, R. J., Brown, T. M., Hygelund, J., et al. 2016, *SPIE Conf. Ser.*, **9908**, 99086X
- Siverd, R. J., Brown, T. M., Barnes, S., et al. 2018, *SPIE Conf. Ser.*, **10702**, 107026C
- Skrutskie, M. F., Cutri, R. M., Stiening, R., et al. 2006, *AJ*, **131**, 1163
- Stassun, K. G., & Torres, G. 2016, *AJ*, **152**, 180
- Stassun, K. G., & Torres, G. 2018, *ApJ*, **862**, 61
- Stassun, K. G., & Torres, G. 2021, *ApJ*, **907**, L33
- Stumpe, M. C., Smith, J. C., Catanzarite, J. H., et al. 2014, *PASP*, **126**, 100
- Swain, M. R., Estrela, R., Roudier, G. M., et al. 2021, *AJ*, **161**, 213
- Tokovinin, A. 2018, *PASP*, **130**, 035002
- Torres, G., Andersen, J., & Giménez, A. 2010, *A&ARv*, **18**, 67
- Twicken, J. D., Chandrasekaran, H., Jenkins, J. M., et al. 2010, *SPIE Conf. Ser.*, **7740**, 77401U
- Twicken, J. D., Catanzarite, J. H., Clarke, B. D., et al. 2018, *PASP*, **130**, 064502
- VanderPlas, J. T. 2018, *ApJS*, **236**, 16
- Winn, J. N., Matthews, J. M., Dawson, R. I., et al. 2011, *ApJ*, **737**, L18
- Wisdom, J. 2006, *AJ*, **131**, 2294
- Wisdom, J., & Holman, M. 1991, *AJ*, **102**, 1528
- Wright, E. L., Eisenhardt, P. R. M., Mainzer, A. K., et al. 2010, *AJ*, **140**, 1868
- Zhang, M., Knutson, H. A., Wang, L., et al. 2021, *AJ*, **161**, 181
- Ziegler, C., Tokovinin, A., Briceño, C., et al. 2020, *AJ*, **159**, 19
- Ziegler, C., Tokovinin, A., Latiolais, M., et al. 2021, *AJ*, **162**, 192

¹ Department of Physics “Ettore Pancini”, University of Naples, Federico II, 80138 Napoli NA, Italy
e-mail: luca.cacciapuoti@eso.org

² European Southern Observatory, Karl-Schwarzschild-Strasse 2, 85748 Garching bei Munchen, Germany

³ Science and Technology Department, Parthenope University of Naples, CDN IC4, 80143 Napoli, Italy

⁴ INAF-Osservatorio Astronomico di Capodimonte, Salita Moraliello, 16, 80131 Napoli, Italy

⁵ INFN, Sezione di Napoli, Strada Comunale Cinthia, 80126 Napoli NA, Italy

⁶ NASA Goddard Space Flight Center, Exoplanets and Stellar Astrophysics Laboratory (Code 667), Greenbelt, MD 20771, USA

⁷ Vanderbilt University, Department of Physics & Astronomy, 6301 Stevenson Center Lane, Nashville, TN 37235, USA

- ⁸ Fisk University, Department of Physics, 1000 18th Avenue N., Nashville, TN 37208, USA
- ⁹ Department of Astronomy, University of Maryland, College Park, MD 20742, USA
- ¹⁰ Department of Astronomy, University of California Berkeley, Berkeley, CA 94720-3411, USA
- ¹¹ Department of Earth and Planetary Sciences, University of California, Riverside, CA 92521, USA
- ¹² SETI Institute, 189 Bernardo Ave, Suite 200, Mountain View, CA 94043, USA
- ¹³ Department of Physics and Astronomy, Bishops University 2600 College St, Sherbrooke, QC J1M 1Z7, Canada
- ¹⁴ Tsinghua International School, Beijing 100084, PR China
- ¹⁵ George Mason University, 4400 University Drive, Fairfax, VA 22030 USA
- ¹⁶ Center for Astrophysics, Harvard & Smithsonian, 60 Garden Street, Cambridge, MA 02138, USA
- ¹⁷ Perth Exoplanet Survey Telescope, Perth, Western Australia, Australia
- ¹⁸ Departamento de Matemática y Física Aplicadas, Facultad de Ingeniería, Universidad Católica de la Santísima Concepción, Alonso de Rivera 2850, Concepción, Chile
- ¹⁹ Caltech/IPAC-NASA Exoplanet Science Institute, 770 S. Wilson Avenue, Pasadena, CA 91106, USA
- ²⁰ NASA Exoplanet Science Institute, Caltech/IPAC, Mail Code 100-22, 1200 E. California Blvd., Pasadena, CA 91125, USA
- ²¹ NASA Ames Research Center, Moffett Field, CA 94035, USA
- ²² Department of Physics, Engineering and Astronomy, Stephen F. Austin State University, 1936 North St, Nacogdoches, TX 75962, USA
- ²³ Cerro Tololo Inter-American Observatory, Casilla 603, La Serena, Chile
- ²⁴ Department of Physics and Astronomy, The University of North Carolina at Chapel Hill, Chapel Hill, NC 27599-3255, USA
- ²⁵ Department of Physics and Kavli Institute for Astrophysics and Space Research, Massachusetts Institute of Technology, Cambridge, MA 3902139, USA
- ²⁶ Harvard-Smithsonian Center for Astrophysics, 60 Garden Street, Cambridge, MA 02138, USA
- ²⁷ Institute of Space Astrophysics and Planetology INAF-IAPS, Via Fosso del Cavaliere 100, 00133 Rome, Italy
- ²⁸ Western Connecticut State University, 181 White Street, Danbury, CT 06810, USA
- ²⁹ Department of Astronomy and Carl Sagan Institute, Cornell University, 122 Sciences Drive, Ithaca, NY 14853, USA
- ³⁰ Proto-Logic LLC, 1718 Euclid Street NW, Washington, DC 20009, USA
- ³¹ Department of Earth, Atmospheric and Planetary Sciences, Massachusetts Institute of Technology, Cambridge, MA 02139, USA
- ³² Kavli Institute for Astrophysics and Space Research, Massachusetts Institute of Technology, Cambridge, MA 02139, USA
- ³³ SETI Institute, Mountain View, CA 94043, USA
- ³⁴ Department of Astrophysical Sciences, Princeton University, Princeton, NJ 08544, USA
- ³⁵ Department of Earth, Atmospheric, and Planetary Sciences, Massachusetts Institute of Technology, Cambridge, MA 02139, USA
- ³⁶ Department of Aeronautics and Astronautics, Massachusetts Institute of Technology, Cambridge, MA 02139, USA
- ³⁷ University of Southern Queensland, Centre for Astrophysics, West Street, Toowoomba, QLD 4350 Australia
- ³⁸ Department of Physics and Kavli Institute for Astrophysics and Space Research, Massachusetts Institute of Technology, Cambridge, MA 02139, USA
- ³⁹ Curtin Institute of Radio Astronomy, Curtin University, Bentley, Western Australia 6102, Australia
- ⁴⁰ Department of Physics and Astronomy, University of New Mexico, 210 Yale Blvd NE, Albuquerque, NM 87106, USA
- ⁴¹ Department of Physics and Kavli Institute for Astrophysics and Space Research, Massachusetts Institute of Technology, Cambridge, MA 02139, USA
- ⁴² University of Maryland, Baltimore County, 1000 Hilltop Circle, Baltimore, MD 21250, USA

Appendix A: DAVE results

In this section we show examples of DAVE results. Figures A.1 and A.2 show the photocenter difference images for the planet candidates as computed in different sectors. The black star indicates the TIC position, and the red circle is the average of measured photocenters for each transit. The white dashed line indicates the TESS target pixel aperture used to extract the light curve. Figures A.3 and A.4 show TESS transit data (first panel), the binned data (second panel), diagnostic plots to check for odd–even effects (third panel), secondary and tertiary eclipses, and positive bumps, as might be produced by false positives (bottom panel). DAVE analysis reports no significant false-positive indicators for TOI 411 *b* and *c*.

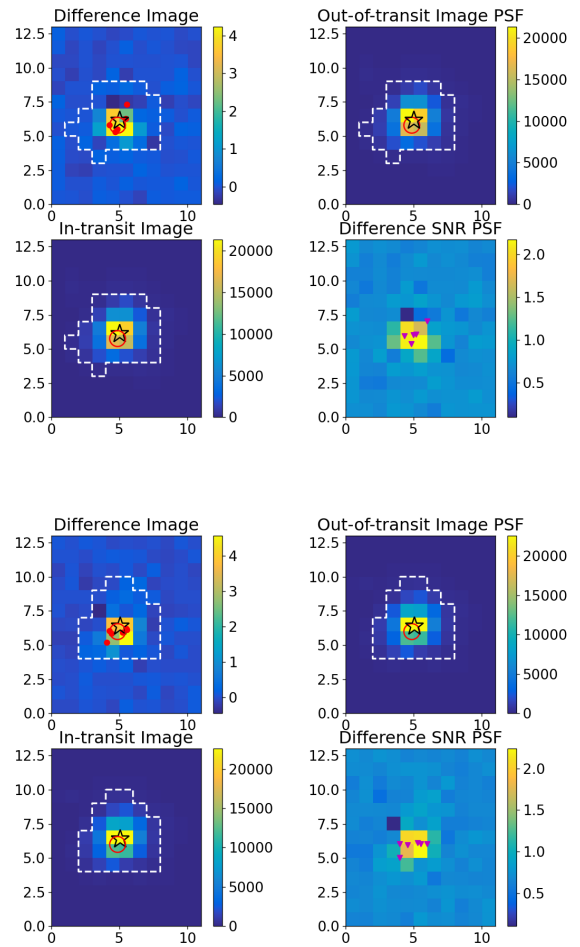


Fig. A.1. DAVE photocenter out-of-transit, in-transit, difference, and difference S/N images for planet b based on TESS sector 3 (upper panel) and 30 (lower panel) data. The axis numbers are expressed in TESS pixels.

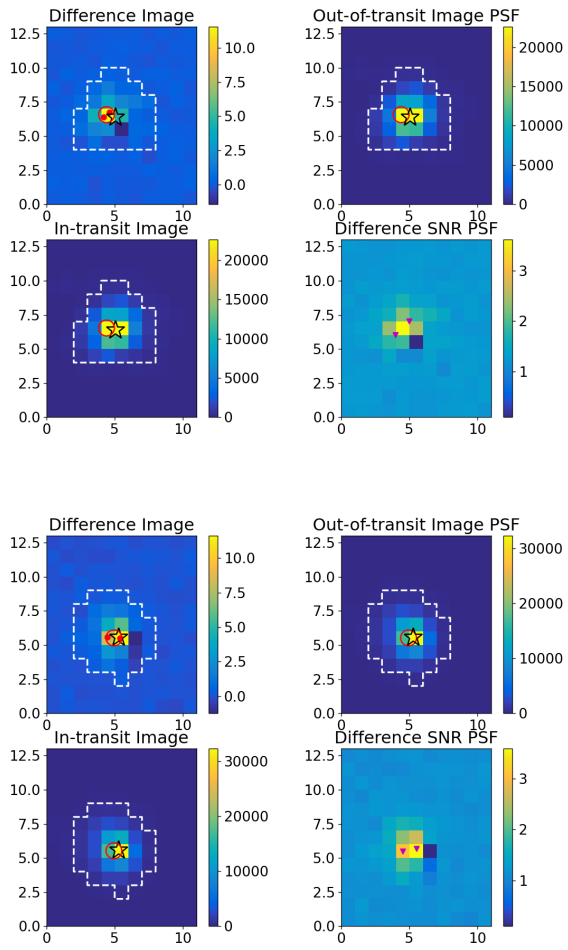


Fig. A.2. DAVE photocenter out-of-transit, in-transit, difference, and difference S/N images for planet c based on sector 30 (upper panel) and 31 (lower panel) data. The axis numbers are expressed in TESS pixels.

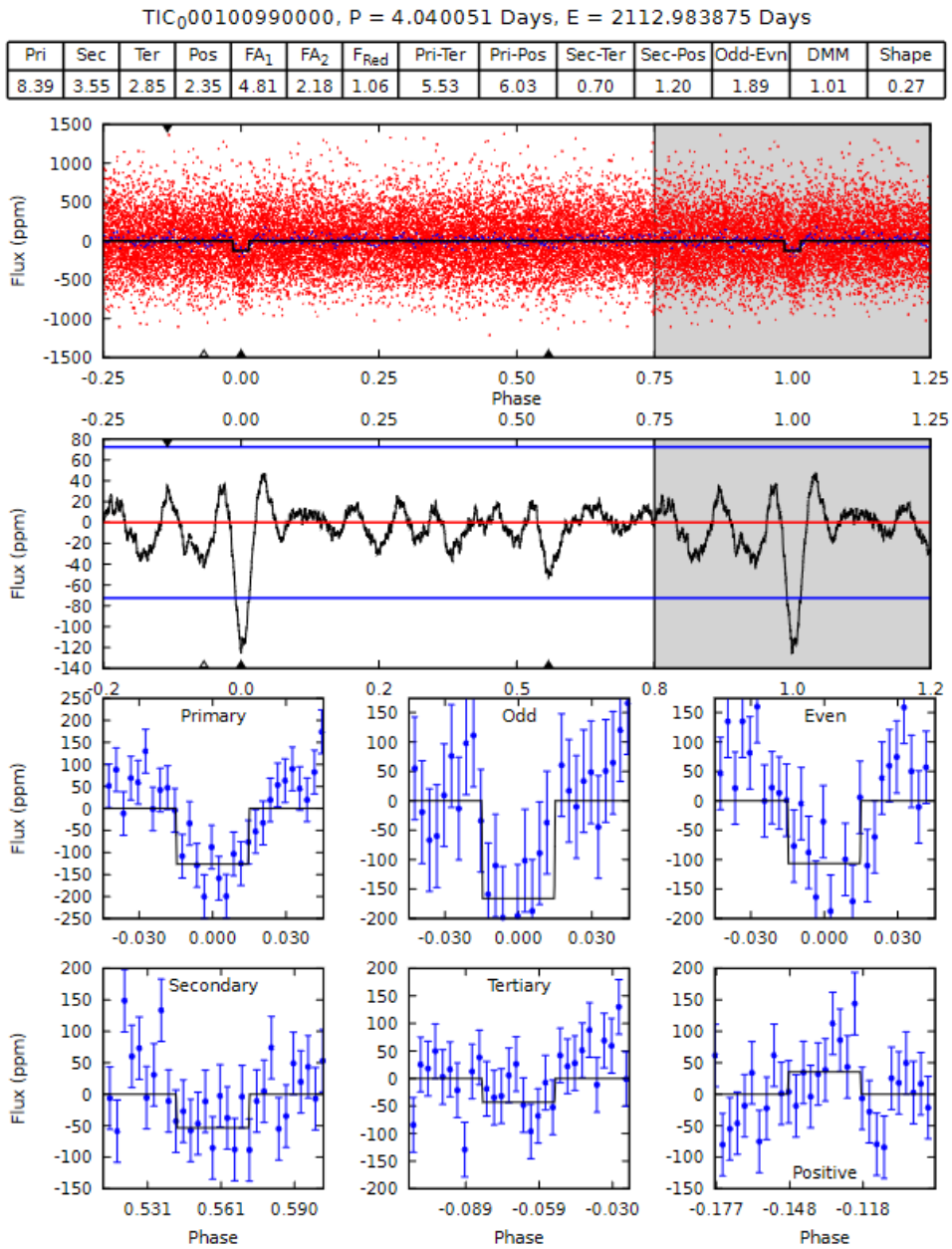


Fig. A.3. DAVE Modelshift for planet b based on TESS data of Sector 30. No significant false-positive indicator is detected.

TIC₀00100990000, P = 9.570000 Days, E = 2142.466499 Days

Pri	Sec	Ter	Pos	FA ₁	FA ₂	F _{Red}	Pri-Ter	Pri-Pos	Sec-Ter	Sec-Pos	Odd-Evn	DMM	Shape
14.5	3.77	3.19	3.27	4.94	2.41	1.06	11.3	11.2	0.58	0.50	0.94	1.00	0.18

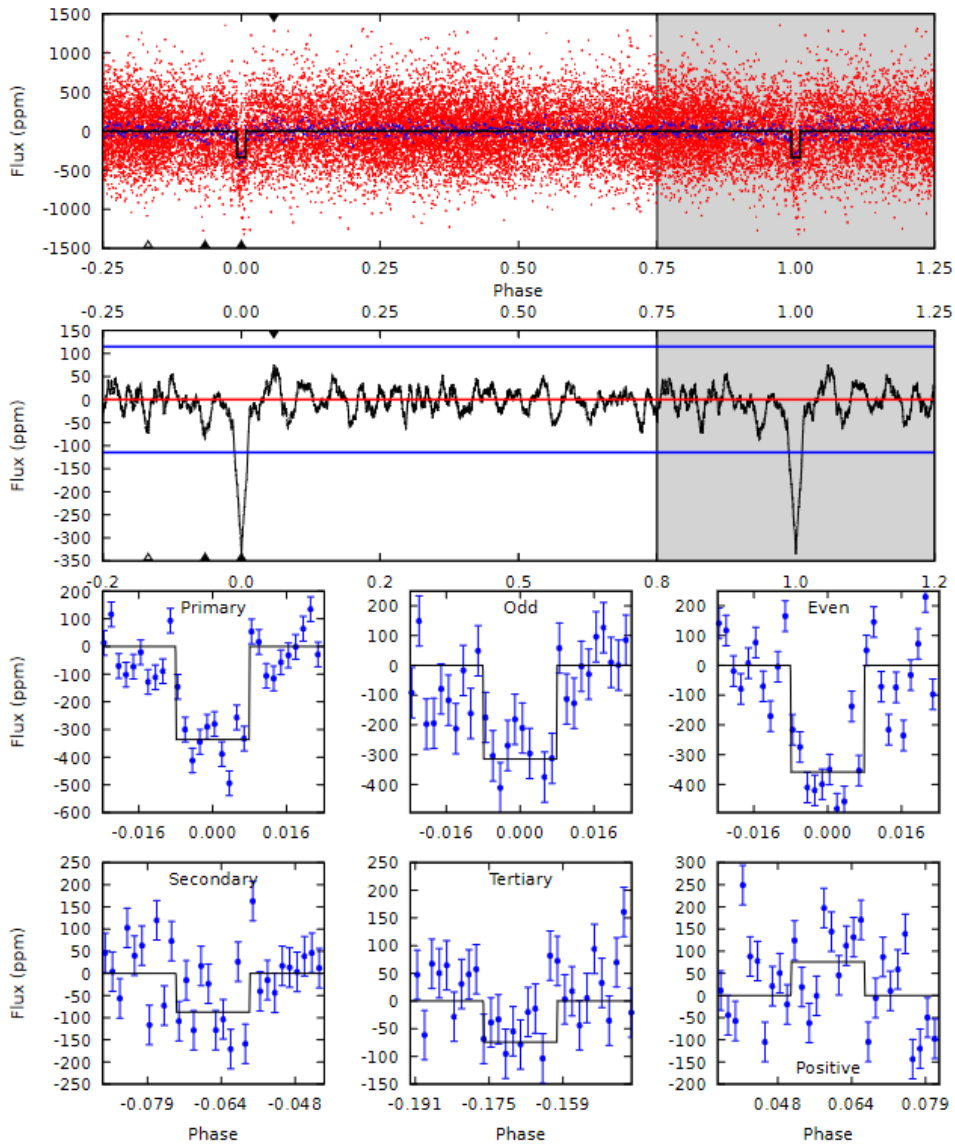


Fig. A.4. DAVE Modelshift for planet c based on TESS data of Sector 31. No significant false-positive indicator is detected.